Control of D-Spacing and Graphitic Defects in Asphaltene-Derived Hard Carbons for Energy Storage

by

Gaoxin Zhang

A thesis submitted in partial fulfillment of the requirements for the degree of

Master of Science

in

Chemical Engineering

Department of Chemical and Materials Engineering

University of Alberta

ABSTRACT

With the increasing demand for energy storage and declining lithium stores around the globe, sodium is emerging as an alternative source due to its natural abundance and similar reaction kinetics and chemical properties to lithium. While sodium-ion and lithium-ion batteries started development at approximately the same time, sodium-ion batteries were cast aside as sodium has a larger ionic radius, leading to incompatibilities with graphite and its interlayer spacing. Asphaltenes are the heaviest components, with a relatively high percentage commonly found in the Alberta Oilsands bitumen. They are currently being explored for their purposes in energy storage as they can form hard carbons after treatment. Asphaltenes are the portion of materials in oil soluble in toluene and insoluble in excess n-heptane. These carbons are an excellent choice for sodium-ion batteries as they have large interlayer spacing, lattice defects, and disorder, which can better accommodate the size of sodium ions. This thesis explores the various treatment conditions used to tailor the interlayer spacing and graphitic defects of asphaltene-derived hard carbons to better accommodate the intercalation of sodium ions during charge/discharge processes for future applications. Conventional graphite has a d-spacing of 0.336 nm, and the results from these experiments have resulted in an extensive range of interlayer spacing ranging from a low of 0.373 nm to a high of 0.392 nm. This increase was accomplished by altering the hold temperature, hold time, and heating rate for the stabilization/oxidation and carbonization processes of asphaltenes to convert them into usable materials for energy storage. The increase in interlayer spacing seen from these results allows for the potential usage of Alberta asphaltenes in sodium-ion batteries.

PREFACE

This is an original work by Gaoxin Zhang. No part of this thesis has been previously published.

Acknowledgements

I want to thank my supervisor, Dr. Weixing Chen, for allowing me to work on this project and supporting me throughout the past two years, no matter the obstacles I faced. He has instilled knowledge, supported me through success and failures, and allowed me to grow and improve. This work could not have been done without his guidance and help.

Lastly, I want to thank my family, friends, and Grace for giving me the love and support I needed to push forward.

TABLE OF CONTENTS

LIST OF TABLES

LIST OF FIGURES

Chapter 1 – Introduction to Asphaltenes and Potential Usage in Batteries

1.1 Background

In modern times, lithium-ion batteries (LIBs) have been the premier form of energy storage. However, due to current energy demand, there is a significant reduction in lithium resources around the globe. Because of this, other methods are being researched to help supply this energy demand. Out of the many possible solutions, sodium-ion batteries (SIBs) are an enticing solution because of their affordable cost due to the abundance of sodium in the earth's crust and the fact that sodium and lithium possess similar chemical properties and reaction mechanisms as they are in the same group 1A in the periodic table [2]. The working mechanism for SIBs is called the "rocking-chair" mechanism, where the sodium ions reversibly migrate between the cathode and anode during charge/discharge processes [3]. This thesis aims to investigate the potential usage of asphaltenes in sodium-ion energy storage.

A vital issue seen in sodium-ion energy storage is the large atomic radius of the sodium ions. Sodium ions have a radius of 1.02Å, which is larger than the radius of lithium ions of 0.76Å [1]. The issue with this is that the large atomic mass leads to slower reaction kinetics due to the constraints on the intercalation of ions between graphite layers, which often results in significant and undesirable volume changes, affecting the cycle life [4]. It also leads to a lower energy density in sodium-ion batteries when compared to lithium-ion batteries.

Electrode material optimization is the most significant challenge for getting SIBs working. Graphite, which is most commonly used in lithium-ion batteries, is unsuitable for SIBs due to the larger ionic radius of sodium, which leads to lower reactivity during charge/discharge processes. Therefore, extensive research has been conducted into different anode materials to help combat this issue. These include carbonaceous materials, alloys, transition metal oxides, sulfides, titanium-based composites, and organic composites [5]. It is believed that the most promising candidates for SIB's anode materials are carbon materials with high structural stability, abundant resources, and cost-effectiveness [1].

While many different feedstocks can be used to form carbon materials, the materials that this thesis focuses on are asphaltenes. Asphaltenes are a by-product of bitumen production commonly found in the Alberta Oilsands. Asphaltenes are defined as the material present in oil that is soluble in toluene and insoluble in excess n-heptane [6]. Three key physical properties are utilized to help differentiate asphaltenes from the other fractions of heavy oil or bitumen. These are insolubility in light alkanes, formation of multicomponent aggregates in crude oil and strong solvents, and strong adherence to a range of surfaces [6].

Solvent deasphalting is a procedure commonly used to help remove asphaltenes from the bitumen stream, which results in reduced viscosity of the remaining bitumen. Asphaltenes, as the by-product of this processing, are widely used as road packing material, gasified to integrate the energy with other operations, or treated by cracking and converted to feedstocks for other conversion processes [6]. While high aromaticity, ash content, molecular weight, and heteroatom content are unfavourable for general production in the oil sands, these aspects can be favourable in usage for energy storage. After treatment, the asphaltenes from the Alberta oilsands bitumen have been proven to be able to form amorphous carbons after carbonization. However, after further analysis, they possess similar characteristics to hard carbons, indicating that there may be a potential for these carbons to be utilized in energy storage as hard carbons.

1.2 Objectives

The primary aim of this project is to investigate a wide range of parameters that could be utilized to modify the interplanar spacing within the d(002) region and defect ratios of hard carbons during the asphaltene conversion process. This research holds significant promise in finding general trends that may enhance the applicability of such materials in energy storage.

The pivotal advantage of manipulating the interplanar spacing is facilitating more effective ion accommodation during the charge/discharge phases of energy storage systems like sodium or lithium-ion batteries. Given that different ions exhibit distinct atomic radii, conventional anode materials for LIBs, like graphite, are unsuitable for certain energy storage technologies, such as

SIBs. The research undertaken in this project seeks to provide general guidance for future work in looking at a broad range of parameters that could most greatly affect the d-spacing and defect ratios found in asphaltene-derived hard carbons. After honing in on specific parameters with additional analyses with greater precision and accuracy, these can be utilized to form asphaltene-derived hard carbon for future energy storage applications.

1.3 Scope of Work

Chapter 2 addresses the treatment process for raw materials to form hard carbons and the reaction mechanisms required to create usable carbon materials for energy storage. It also studies the literature on functional energy systems for hard carbons, different materials in sodium-ion batteries, and reasons why sodium-ion storage is not widely used commercially.

As these Alberta asphaltenes have already been used in forming carbon fibres, a similar approach for treatment will be used for the asphaltene powder to create tailorable hard carbons for energy storage. Chapter 3 covers the experimental procedure, raw material information, and analysis methods utilized in future sections. Chapter 4 investigates the effect of particle size of the raw material, followed by Chapter 5, manipulation of oxidation parameters and lastly, Chapter 6, which studies the alteration of carbonization parameters. Each chapter thoroughly explores the effects of these variables on the interplanar spacing, elemental composition and defect ratios.

1.4 References

[1] R. Zhao, N. Sun, and B. Xu, “Recent Advances in Heterostructured Carbon Materials as Anodes for Sodium-Ion Batteries,” *Small structures*, vol. 2, no. 12, Oct. 2021, doi: https://doi.org/10.1002/sstr.202100132.

[2] F. Soto *et al.*, “Tuning the Solid Electrolyte Interphase for Selective Li- and Na-Ion Storage in Hard Carbon,” vol. 29, no. 18, pp. 1606860–1606860, Mar. 2017, doi: https://doi.org/10.1002/adma.201606860.

[3] Z. Li *et al.*, “Mechanism of Na-Ion Storage in Hard Carbon Anodes Revealed by Heteroatom Doping,” vol. 7, no. 18, pp. 1602894–1602894, May 2017, doi: https://doi.org/10.1002/aenm.201602894.

[4] M. I. Jamesh and A. S. Prakash, “Advancement of technology towards developing Na-ion batteries,” *Journal of Power Sources*, vol. 378, pp. 268–300, Feb. 2018, doi: https://doi.org/10.1016/j.jpowsour.2017.12.053.

[5] W. Zhang, F. Zhang, F. Ming, and H. N. Alshareef, “Sodium-ion battery anodes: Status and future trends,” *EnergyChem*, vol. 1, no. 2, p. 100012, Sep. 2019, doi: https://doi.org/10.1016/j.enchem.2019.100012.

[6] J. G. Speight, “A Review of: ‘The Chemistry of Alberta Oil Sands Bitumens and Heavy Oils,’” *Energy Sources*, vol. 27, no. 8, pp. 780–780, Jun. 2005, doi: https://doi.org/10.1080/00908310590967283.

Chapter 2 – Literature Review

2.1 Introduction

To enhance our knowledge of developing low-cost and scalable hard carbons, it is critical to investigate the variables in each process relevant to altering the interplanar spacing. To create suitable anode materials, the following areas need to be considered and are therefore included in this chapter:

- General information on asphaltenes
- Usage of asphaltenes in batteries
- Conversion of carbonaceous materials
- Current materials used for anode materials for sodium-ion batteries
- Methods to alter the interplanar spacing of carbon-based anode materials
- Chemistry related to the oxidation and carbonization process for the conversion of asphaltenes (or related materials) to carbons

2.2 Additional Information and Background About Asphaltenes

Asphaltenes are arguably one of the most complex fractions derived from petroleum, which has been the subject of many controversies due to its challenging molecular characterization. Between the 1970s and the 2000s, it was discussed whether asphaltene molecules possessed a high (>4000 g/mol) or low (<1200 g/mol) molecular weight [1]. There is a consensus that asphaltene monomers are low molecular weight species with the most abundant masses between 250g/mol and 1200 g/mol with an average molecular weight of ~700 g/mol [1]. Today, questions about asphaltene chemistry focus on the molecular structure, either being a single-core or "island" versus multicore of "archipelago," and the nature of the molecular interaction involved in asphaltene self-aggregation, which is still a contested topic. [1] Even with this contested topic, it is generally agreed upon that asphaltenes have three key components: an aromatic core, heteroatoms, and alkyl side chains [22]. Of the many different models of asphaltenes, the most widely used is the Yen-Mullins Model, which can be seen in Figure 1.

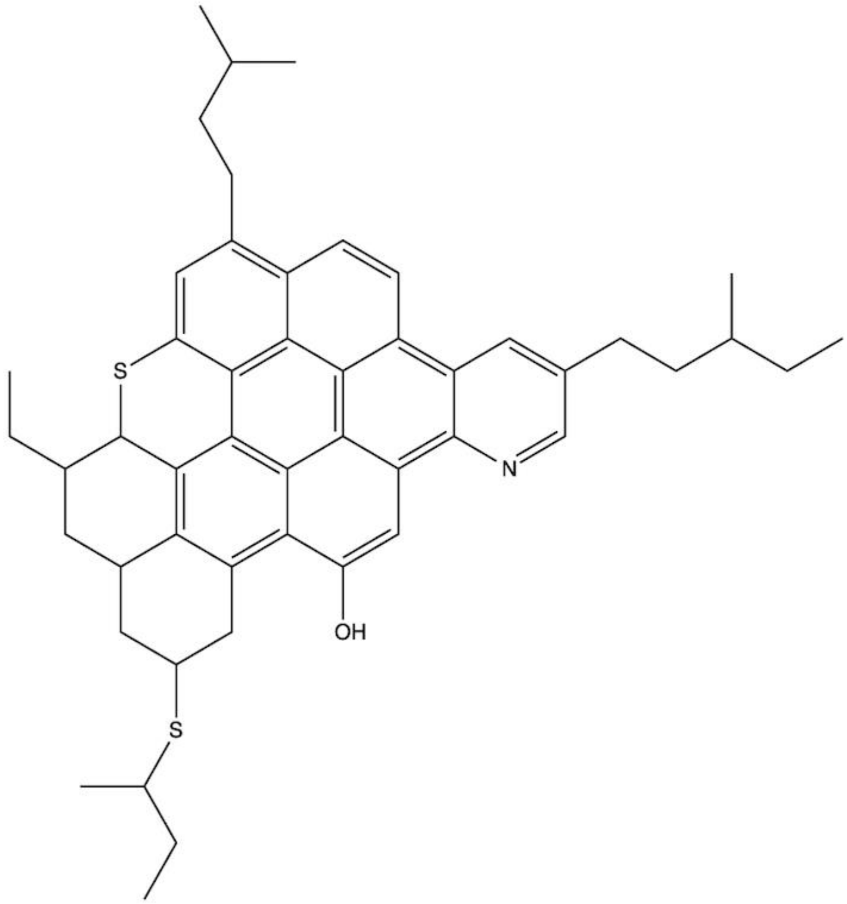

Figure 1: Asphaltene molecule based on the Yen-Mullins model

Crude oil sourced naturally cannot be directly used as it must undergo extensive processing to be made into light fuels to power vehicles and for petrochemicals for various industries [9]. The main goal of the refinement process revolves around yielding the most significant number of fuels and chemicals from the crude oil. To accomplish this, valuable and invaluable products/by-products must be separated to be commercially used. The refinery process is typically categorized into a separation and conversion process. The heavy residue from the separation process, like distillation, is asphalt, a mixture of saturates, aromatics, resins, and asphaltenes [9]. The typical structure of the fractions can be found below.

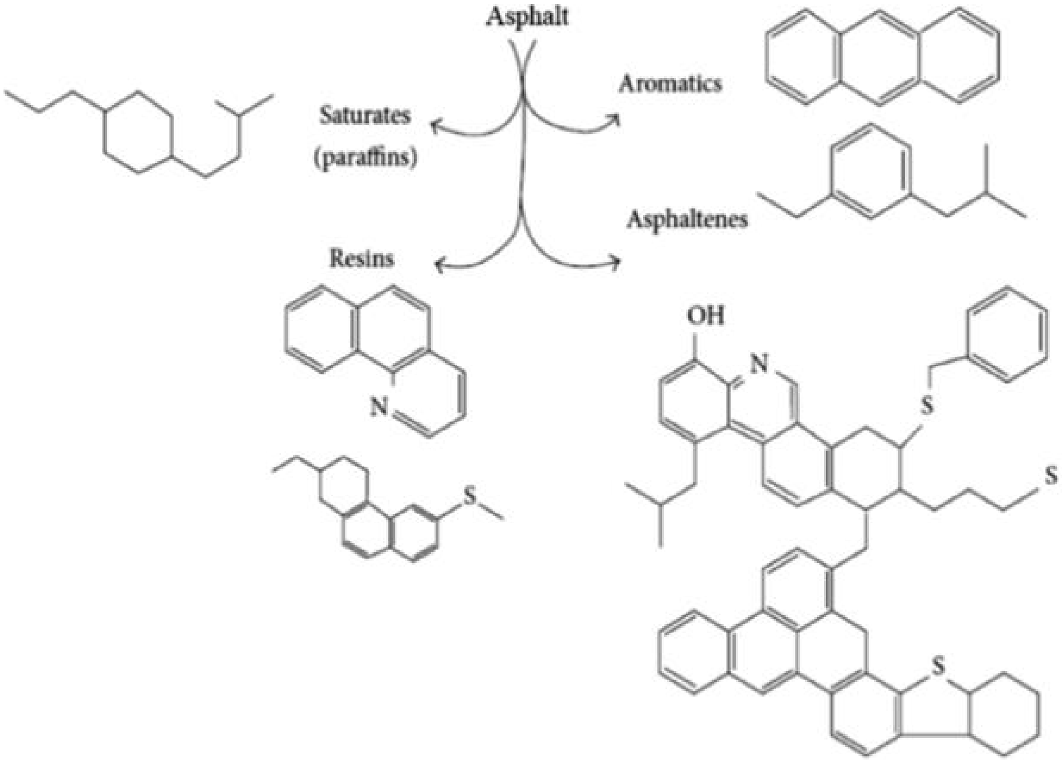

Figure 2: Example of asphalt fractions [2]

Most of these components are comprised of polycyclic aromatic hydrocarbons (PAHs), which can form large graphitic domains. This leads to carbonaceous materials produced from these precursors having excellent conductivity and flexibility [9].

Asphaltenes possess a problematic nature of aggregation and precipitation, which results in the plugging of well bores and flowlines during crude oil processing. These natures originate from hydrogen bond forces, aromatic pi-pi stacking forces, polarity induction forces, and electrostatic attraction, causing the formation of coke-like precursors [2]. This result impedes the processing and lowers the economic value of crude oil. While these characteristics may be a detriment to the oil refining process, they can be beneficial in other applications of asphaltenes.

Due to the large amount of oil being produced globally, the undesired by-product, asphaltenes, can be found in large quantities, currently have little market value, and are generally disposed of. The separated waste is injected into tailings ponds, causing environmental issues, which leads to the idea that utilizing asphaltenes in different areas and applications would be able to address the ecological consequences seen with this by-product in the crude oil industry [2].

There is interest in different applications, such as the polymer industry, nanomaterial synthesis, electronics, and emulsions and interfaces. In this thesis, we will focus on using asphaltenes in energy storage.

2.3 Usage of Asphaltenes in Batteries

2.3.1 Lithium-ion Batteries

Lithium-ion batteries are the most widely used due to their light weight and high energy density. This can be seen most prominently in electronic devices and electric cars. These batteries work through a “rocking chair” method where lithium-ions are intercalated between the anode and the cathode for energy storage [10]. Graphite is typically used as the primary material in the anode material as the interlayer spacing between two graphene sheets provides an optimal location for lithium ions to intercalate into. Petroleum coke is primarily used as the precursor for graphite, and after calcination, the moisture and volatiles in the coke are mostly removed [9]. After a thermal annealing process of around 2800^{o}C, the artificial graphite is ready to be used [9].

Hard carbons derived from asphaltenes are a potential solution for finding alternatives to conventional graphite in LIBs. The hard carbons are typically formed using pre-oxidized or solvent-extracted asphalt [10]. This allows for the asphalt to be thermally stable at elevated temperatures and reduces the amount of fusing seen, which leads to the retention of its original structure that is more disordered. Compared to conventional graphite anodes with only one insertion and extraction path, hard carbons exhibit a three-dimensional diffusion path, significantly increasing the rate capability [9]. Overall, the performance of these carbon materials for lithium storage is determined by many factors. These include crystallinity, particle size, porosity, morphology, hetero-species, etc.

2.3.2 Sodium-ion Batteries

Sodium-ion batteries are a promising alternative to lithium-ion batteries as aluminum foil can be used as the current collector for SIBs instead of the more expensive copper foil in LIBs due to the higher redox potential of sodium, which makes SIBs more economically viable [9]. While this may be beneficial, it is also an issue as the higher redox potential of sodium results in the thermodynamically unfavourable formation of sodium intercalated graphite [9]. Initial studies on graphite since the 1980s showed limited success in accommodating sodium ions, leading to subpar capacity results [5].

Material choice is limited for the anode as the material must be able to accommodate the larger size of Na ions (1.02A) and its high ionization potential of (5.139 eV) [16]. Therefore, hard carbons have been proposed as an anode material for sodium-ion batteries due to internal micropores, d-spacing, and defects, which benefit sodium storage and enable a higher specific capacity [11].

2.4 Conversion Methods of Carbonaceous Materials for Energy Storage Applications

2.4.1 Direct Carbonization of Biomass and Pitch

Direct carbonization involves the thermal processing of raw materials in an inert environment to produce hard carbons. A resurgence of interest in 2011 steered research towards hard carbons synthesized from organic materials like sucrose, cellulose, wood, argan shells, and peanut shells, revealing better sodium insertion capabilities [5]. Biomass, rich in cellulose and hemicellulose, decomposes between 200°C and 400°C, whereas lignin, a complex aromatic polymer, breaks down over a wider temperature range, from 250°C to 900°C [3]. The resultant structures are inherently disordered, leading to the formation of hard carbons. On the other hand, pitch, while typically leading to graphitic structures due to its polycyclic aromatic nature, can be optimized for SIBs through controlled heat treatments at 400-500°C to produce hard carbons, which are disordered.

2.4.2 Co-Carbonization: Integrating Biomass with Pitch

In the co-carbonization approach, biomass and pitch are combined to utilize the beneficial aspects of both materials. Biomass-derived components tend to result in bulky, amorphous carbons, while pitch is conducive to forming layered, graphitic structures. Co-carbonizing these materials blends the non-graphitizable and graphitizable properties, potentially enhancing the storage capacity due to a mix of accessible ion intercalation sites [3].

2.4.3 Activation Process

Activation is critical in developing porous carbon materials with high specific surface areas. This is typically achieved by calcining carbon precursors in the presence of chemical activators, such as KOH, under inert conditions. The resulting activation process etches the carbon framework, creating a rich pore structure with micro- and mesopores beneficial for adsorption and energy storage processes [3].

2.4.4 Template Method for Structured Carbons

The template method allows for the fabrication of carbon materials with precise and tailored structures. The precursor material is impregnated with a template with a defined morphology. Subsequently, heat treatment at elevated temperatures results in carbon materials that inherit these predetermined shapes, which is helpful for energy storage applications [3].

2.5 Current Materials Used for Anode Materials for Sodium-ion Batteries

An array of anode materials is being explored, from carbons and alloys to metal oxides and 2-D materials. These different materials can store sodium ions through either insertion/intercalation, conversion, or alloying reactions.

To be an optimal SIB anode, the active material in the anode material must fulfill the following requirements [18]:

1. Low atomic weight, low density, and the ability to accommodate a large number of sodium ions.
2. Potential close to pure sodium metal, which does not change with sodium content so that the overall working voltage is not lower than the cathodic voltage.
3. Must not react or show dissolution in the electrolyte.
4. Must be environmentally friendly and possess high electronic and ionic conductivity.

2.5.1 Soft Carbons

Soft carbons possess relatively well-ordered layer structures and high degrees of graphitization, correlating to superior electrical conductivity. The precursors for forming soft carbons typically include aromatic compounds and polymers commonly sourced from petroleum coke and other carbonaceous products.

Despite the low-strain regions and minimal defects enhancing electrical conductivity, soft carbons have limitations. The organized stacking of carbon layers poses challenges for inserting and extracting sodium ions due to restricted active sites and difficulty in ion transport. The interlayer gap in these structures, similar to graphite, is usually around 0.336 nm. It needs to be more accommodating for the sodium ions with their larger ionic radius of 0.102 nm to increase sodium-ion storage capacity [10]. Soft carbons generally show a lower storage capability, ranging from 100 to 250 mAh/g, owing to the limited number of active sites [10]. Therefore, research in soft carbons revolves around boosting the number of active sites. This involves modifying the carbon structure to incorporate porous networks and adjusting the interlayer spacing to facilitate a more hospitable environment for sodium-ion intercalation and improve overall storage capacity [10].

2.5.2 Hard Carbons

Hard carbon materials are characterized by randomly aligned graphene crystallites with significant disorder and expanded interlayer spacing [10]. These characteristics have demonstrated a high potential for sodium-ion battery applications. These carbons help facilitate the insertion and extraction of sodium ions within the disordered graphene layers, often delivering a reversible capacity of ~300mAh/g, as indicated by recent studies [10]. Remarkably, some of these materials can maintain their structural disarray and relatively low crystallinity even after undergoing graphitization at temperatures exceeding 3000°C [10].

The economic viability of hard carbons is another noteworthy advantage due to readily available and diverse precursors such as renewable biomass, synthetic resins, sugars, and various industrial or agricultural by-products [12]. These precursors are rich in carbon and contain oxygen, hydrogen, and multiple heteroatoms like nitrogen, sulphur, and phosphorus [10]. The synthesis process of hard carbons is relatively straightforward and scalable, predominantly involving direct pyrolysis of the raw materials.

Despite the many advancements in hard carbons, many issues still need to be fixed to integrate hard carbons into SIBs fully. The formation of the solid-electrolyte interphase (SEI) layer is one of the main issues. The increased surface area and more significant defects of hard carbons can cause an overabundance of SEI layer formation, leading to the irreversible trapping of sodium during the first charge cycle and significantly reducing initial coulombic efficiency (ICE) [13]. Additional concerns arise from the formation of energetically unfavourable compounds during sodium intercalation, particularly within the SEI layer, which is also influenced by the solvation energy [5]. It was generally found that the irreversible capacity loss decreases with a decrease in specific surface area and porosity of hard carbon materials. However, no straightforward correlations have been established between the specific surface area, porosity, and irreversible capacity [14].

Moreover, the randomly aligned graphene crystallites and their intrinsic low electrical conductivity decrease the rate performance. Another industrial concern is the relatively low yield of the precursor materials, often under 30%, which poses a significant hurdle to the large-scale production and commercialization of hard carbons [14].

2.5.3 Amorphous Carbons

Amorphous carbon structures possess characteristics of both hard and soft carbons. These materials, which fall under the category of amorphous carbons, boast a low defect ratio and crystallinity that encompasses both high-strain (disordered) and low-strain (graphitic) regions, promoting effective electron transport [10].

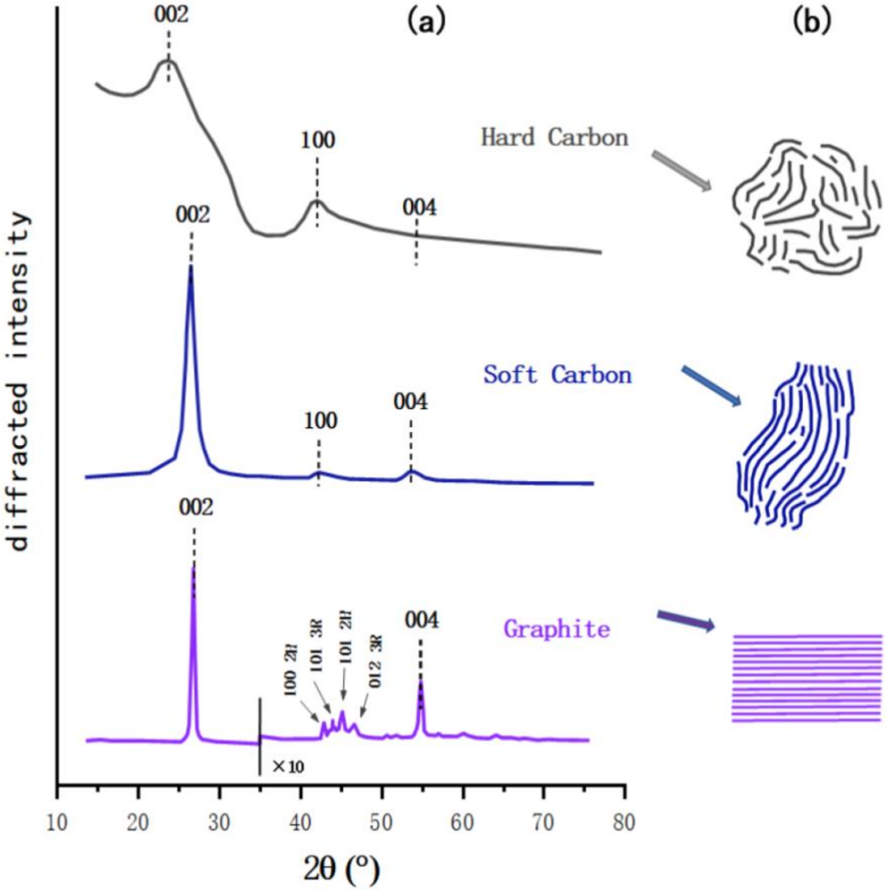

Figure 3: Examples of different kinds of XRD patterns for different carbon structures [23]

Figure 3 depicts the differences of each type of carbon and how we can distinguish between them.

2.5.4 Alloying Materials

Sodium can form alloys with elements from groups 14 and 15 of the periodic table, which means these materials can be used as anode material for SIBs. This includes Si, Ge, Sn, Pb, P, Sb, and Bi. Each element's singular atom can form an alloy with more than one sodium ion at an average operation potential lower than 1V against Na/Na+ [18].

The domain of alloys as anode materials is emerging, attributed to their large energy density and lower redox potentials. Notable for their ability to form Na-metal-alloy phases, alloys such as Si, Ge, Sn, Pb, and Sb are recognized for their enhanced capacities through alloying with sodium, as pointed out by Chevier and Ceder [5].

Sn, Sb, and P are the most widely studied materials for the anode, as Pb and Bi suffer from significant volumetric changes. The Na alloy anode materials often provide a high reversible capacity of >500mAh/g but suffer from substantial volume changes, up to 400%, during the charge and discharge phases [16]. This results in the exfoliation and inactivation of the anode, along with poor cycling stability.

2.5.5 Metal Oxides

Metal oxides are another great potential candidate for Na-ion battery anodes because of their high theoretical capacities. They undergo either an insertion or alloying reaction followed by a conversion reaction. However, a key issue is storing more than one sodium ion, as additional atoms lead to significant volumetric changes. Metal oxides based on conversion-alloying materials typically used include tin, antimony, etc.; conversion materials include iron, nickel, cobalt, molybdenum, copper, and manganese [18].

Unfortunately, their high-capacity potential, which is usually harnessed at lower current densities, is hindered by low conductivity and the necessity for structural reorganization, which is energy-intensive [5]. Like silicon in Li-ion batteries, metal oxides are prone to volume changes during intercalation, risking pulverization and cracking, negatively affecting battery performance, capacity, and rate capability [5].

2.6 Methods to Alter the Interplanar Spacing and Improve Performance of Carbon-Based Anode Materials

Doping with heteroatoms such as nitrogen (N), sulfur (S), phosphorus (P), and boron (B) is a well-documented strategy to increase the interlayer distances in carbon-based materials. Tang et al. demonstrated that C_3N_4-derived N-doped graphene, synthesized with polyvinylpyrrolidone (PVP), achieved adjustable interplanar spacings ranging from 0.34nm to 0.45nm, which were attributed to varying nitrogen content [6]. Zou et al. extended this concept using S, N-codoped carbon nanosheets to create tunable interlayer distances from 0.37nm to 0.41nm [7]. The doping process expands the lattice and introduces a desirable disorder within the carbon structure, which can enhance electrical conductivity [17].

Lou et al. further expanded on these findings by observing that increased spacing between graphene sheets, achieved via heteroatom expansion, led to higher battery capacities [20]. This increased spacing allows for more efficient sodium ion intercalation, which is crucial for SIBs. The disorder introduced by heteroatom doping disrupts the regularity of the graphite layers, preventing restacking and thereby maintaining wider interlayer spacings conducive to ion transport.

Additionally, the effect of pyrolysis temperature on the evolution of hard carbon structures has been extensively studied. A general trend has been noted: as the pyrolysis temperature increases, the surface area and porosity tend to decrease, alongside a reduction in the number of defects due to a higher degree of graphitization [14]. This relationship indicates that higher temperatures can enhance conductivity through increased graphitization. However, they may also reduce the material's ability to host sodium ions due to decreased porosity and interplanar spacing.

Thermally expanded graphite has been produced using modified Bordie and Hummers methods, increasing interlayer distances [19]. By utilizing various annealing temperatures ranging from

700°C to 1600°C, researchers have reported interlayer spacings that span from 0.362 nm to 0.346 nm, respectively [20]. This showcases thermal treatment's ability to alter graphite's interlayer spacing.

2.7 Chemistry Related to the Oxidation and Carbonization Process for the Conversion of Raw Materials to Carbonaceous Materials

The transformation of raw materials into carbonaceous structures for energy storage entails a two-step heat-treatment process: oxidative stabilization and carbonization. Specific chemical reactions and structural changes characterize each stage. Mechanisms of oxidation and carbonization for pitch can be utilized to help understand asphaltenes as they possess similar characteristics.

2.7.1 Oxidative Stabilization Chemistry

Oxidative stabilization is the initial step that allows the raw material to cross-link, enabling it to endure subsequent higher-temperature treatments. This phase is crucial in preventing melting and fusion while minimizing the expulsion of volatile carbon side chains, which leads to an increased carbon yield post-carbonization [21].

The weight-gain reactions during oxidative stabilization involve the removal of methylene hydrogens followed by an attack of molecular oxygen [22]. The formation and decomposition of a hydroperoxide intermediate produce water and ketone functionality, which results in a net weight gain [22]. These reactions occur rapidly at the initial stages of oxidation without the need for excessively high temperatures.

The subsequent weight-loss reactions occur at higher temperatures or extended oxidation periods through thermally induced homolytic bond scissions [22]. This process allows oxygen insertion between molecules, forming oxygen-containing cross-links identified as mostly ester and anhydride-type functionalities [21]. The weight loss is attributed to concerted decarboxylationtype degradations that remove carbon content from the raw material in carbon dioxide and carbon monoxide without reorganizing the lattice [22].

2.7.2 Carbonization Chemistry

Carbonization is conducted under an inert gas to prevent combustion and accelerate the elimination of other elements in the form of N_2, O_2, H_2 gases and other structural impurities while simultaneously increasing the carbon content [8]. The oxidized material primarily releases carbon dioxide, carbon monoxide, water, hydrogen gas, and small quantities of oligomers, methane, and light alkanes during carbonization [21]. This further decreases the concentration of the remaining non-carbonizable aliphatic content. Increased aliphatic content is also achieved by increasing the number of oxygenated cross-links between pitch molecules that undergo degradation by a concerted mechanism during carbonization [21]. Retaining the natural structure of the raw material during this process is achieved as oxidized pitches, which have largely lost their aliphatic content during oxidation, are less susceptible to melting during carbonization [21].

2.8 References

[1] M. L. Chacón-Patiño *et al.*, “Lessons Learned from a Decade-Long Assessment of Asphaltenes by Ultrahigh-Resolution Mass Spectrometry and Implications for Complex Mixture Analysis,” vol. 35, no. 20, pp. 16335–16376, Oct. 2021, doi: https://doi.org/10.1021/acs.energyfuels.1c02107.

[2] M. Kamkar and G. Natale, “A review on novel applications of asphaltenes: A valuable waste,” *Fuel*, vol. 285, p. 119272, Feb. 2021, doi: https://doi.org/10.1016/j.fuel.2020.119272.

[3] D. Alvira, D. Antorán, and J. J. Manyà, “Plant-derived hard carbon as anode for sodium-ion batteries: A comprehensive review to guide interdisciplinary research,” *Chemical Engineering Journal*, vol. 447, p. 137468, Nov. 2022, doi: https://doi.org/10.1016/j.cej.2022.137468.

[4] P.-Y. Zhao, J.-J. Tang, and C. Wang, “A low-cost attempt to improve electrochemical performances of pitch-based hard carbon anodes in lithium-ion batteries by oxidative stabilization,” *Journal of Solid State Electrochemistry*, vol. 21, no. 2, pp. 555–562, Sep. 2016, doi: https://doi.org/10.1007/s10008-016-3406-1.

[5] S. Mukherjee, S. Bin Mujib, D. Soares, and G. Singh, “Electrode Materials for High-Performance Sodium-Ion Batteries,” *Materials*, vol. 12, no. 12, p. 1952, Jun. 2019, doi: https://doi.org/10.3390/ma12121952.

[6] Y. Tang, X. Wang, J. Chen, X. Wang, D. Wang, and Z. Mao, “PVP-assisted synthesis of g–C3N4–derived N-doped graphene with tunable interplanar spacing as high-performance lithium/sodium ions battery anodes,” *Carbon*, vol. 174, pp. 98–109, Apr. 2021, doi: https://doi.org/10.1016/j.carbon.2020.12.010.

[7] G. Zou, H. Hou, G. Zhao, Z. Huang, P. Ge, and X. Ji, “Preparation of S/N-codoped carbon nanosheets with tunable interlayer distance for high-rate sodium-ion batteries,” *Green Chemistry*, vol. 19, no. 19, pp. 4622–4632, 2017, doi: https://doi.org/10.1039/c7gc01942d.

[8] İ. Gergin, E. Ismar, and A. S. Sarac, “Oxidative stabilization of polyacrylonitrile nanofibers and carbon nanofibers containing graphene oxide (GO): a spectroscopic and electrochemical study,” *Beilstein Journal of Nanotechnology*, vol. 8, pp. 1616–1628, Aug. 2017, doi: https://doi.org/10.3762/bjnano.8.161.

[9] H. Hu and M. Wu, “Heavy oil-derived carbon for energy storage applications,” *Journal of materials chemistry. A, Materials for energy and sustainability*, vol. 8, no. 15, pp. 7066–7082, Jan. 2020, doi: https://doi.org/10.1039/d0ta00095g.

[10] R. Zhao, N. Sun, and B. Xu, “Recent Advances in Heterostructured Carbon Materials as Anodes for Sodium-Ion Batteries,” *Small structures*, vol. 2, no. 12, Oct. 2021, doi: https://doi.org/10.1002/sstr.202100132.

[11] D. Saurel, B. Orayech, B. Xiao, D. Carriazo, X. Li, and T. Rojo, “From Charge Storage Mechanism to Performance: A Roadmap toward High Specific Energy Sodium-Ion Batteries through Carbon Anode Optimization,” *Advanced Energy Materials*, vol. 8, no. 17, p. 1703268, Mar. 2018, doi: https://doi.org/10.1002/aenm.201703268.

[12] K. Yu, X. Wang, H. Yang, Y. Bai, and C. Wu, “Insight to defects regulation on sugarcane waste-derived hard carbon anode for sodium-ion batteries,” *Journal of Energy Chemistry*, vol. 55, pp. 499–508, Apr. 2021, doi: https://doi.org/10.1016/j.jechem.2020.07.025.

[13] C. Bommier and X. Ji, “Electrolytes, SEI Formation, and Binders: A Review of Nonelectrode Factors for Sodium-Ion Battery Anodes,” *Small*, vol. 14, no. 16, p. 1703576, Jan. 2018, doi: https://doi.org/10.1002/smll.201703576.

[14] P. Liu, Y. Li, Y.-S. Hu, H. Li, L. Chen, and X. Huang, “A waste biomass derived hard carbon as a high-performance anode material for sodium-ion batteries,” *Journal of Materials Chemistry A*, vol. 4, no. 34, pp. 13046–13052, 2016, doi: https://doi.org/10.1039/c6ta04877c.

[15] L. Xiao *et al.*, “Low-Defect and Low-Porosity Hard Carbon with High Coulombic Efficiency and High Capacity for Practical Sodium Ion Battery Anode,” *Advanced Energy Materials*, vol. 8, no. 20, p. 1703238, Mar. 2018, doi: https://doi.org/10.1002/aenm.201703238.

[16] W. Li, S.-L. Chou, J.-Z. Wang, J. H. Kim, H.-K. Liu, and S.-X. Dou, "$Sn_{4+x}P_3$@ Amorphous Sn-P Composites as Anodes for Sodium-Ion Batteries with Low Cost, High Capacity, Long Life, and Superior Rate Capability," *Advanced Materials*, vol. 26, no. 24, pp. 4037–4042, Apr. 2014, doi: https://doi.org/10.1002/adma.201400794.

[17] W. Chen, M. Wan, Q. Liu, X. Xiong, F. Yu, and Y. Huang, "Heteroatom-Doped Carbon Materials: Synthesis, Mechanism, and Application for Sodium-Ion Batteries," *Small Methods*, vol. 3, no. 4, p. 1800323, Oct. 2018, doi: https://doi.org/10.1002/smtd.201800323.

[18] T. Perveen, M. Siddiq, N. Shahzad, R. Ihsan, A. Ahmad, and M. I. Shahzad, "Prospects in anode materials for sodium ion batteries - A review," *Renewable and Sustainable Energy Reviews*, vol. 119, p. 109549, Mar. 2020, doi: https://doi.org/10.1016/j.rser.2019.109549.

[19] M. Cabello *et al.*, "On the Reliability of Sodium Co-Intercalation in Expanded Graphite Prepared by Different Methods as Anodes for Sodium-Ion Batteries," *Journal of The Electrochemical Society*, vol. 164, no. 14, pp. A3804–A3813, Jan. 2017, doi: https://doi.org/10.1149/2.0211714jes.

[20] W. Luo *et al.*, "Electrochemically Expandable Soft Carbon as Anodes for Na-Ion Batteries," *ACS Central Science*, vol. 1, no. 9, pp. 516–522, Nov. 2015, doi: https://doi.org/10.1021/acscentsci.5b00329.

[21] J. Drbohlav and William, "The oxidative stabilization and carbonization of a synthetic mesophase pitch, part I: The oxidative stabilization process," vol. 33, no. 5, pp. 693–711, Jan. 1995, doi: https://doi.org/10.1016/0008-6223(95)00011-2.

[22] M. Hassanzadeh and M. Abdouss, "Essential role of structure, architecture, and intermolecular interactions of asphaltene molecules on properties (self-association and surface activity)," *Heliyon*, vol. 8, no. 12, p. e12170, Dec. 2022, doi: https://doi.org/10.1016/j.heliyon.2022.e12170.

[23] L. Liu, Y. Tian, A. Abdussalam, M. R. H. S. Gilani, W. Zhang, and G. Xu, “Hard Carbons as Anodes in Sodium-Ion Batteries: Sodium Storage Mechanism and Optimization Strategies,” *Molecules*, vol. 27, no. 19, p. 6516, Oct. 2022, doi: https://doi.org/10.3390/molecules27196516.

Chapter 3 – Experimental & Characterization Methods

3.1 Introduction

This section overviews the experimental procedures and analytical techniques employed to synthesize and characterize asphaltene-derived hard carbons. Given the standardized treatment processes across all steps, a consolidated description of the methods is presented.

Originating from the Alberta's oilsands, bitumen was subjected to a series of treatments by Thread Innovations. The initial step involved a solvent extraction to isolate the high molecular weight components. After this, a purification process was conducted to eliminate low molecular weight fractions, leading to asphaltenes with specific physical properties dubbed SVR2-97. The primary characteristics of SVR2-97 are detailed in Table 1.

Table 1: CHNS results for SVR2-97

Softening Point (°C)	**Weight Measured (g)**	**CHNS**					
		N (wt%)	**C (wt%)**	**H (wt%)**	**S (wt%)**	**Sum (wt%)**	**Estimated O and/or residues (wt%)**
245	2.37	1.50	88.52	5.69	3.34	99.05	0.95

The elemental composition of SVR2-97 is predominantly carbon (88.52%), suggesting a potential to form carbonaceous materials. The presence of heteroatoms, including nitrogen, sulfur, oxygen and trace elements such as vanadium and nickel, also characterizes the material. The concentration of these elements may vary based on the location of extraction. The softening point of SVR2-97 is relatively low, at 245°C. SVR2-97 requires oxidative stabilization. Oxidative stabilization serves to cross-link the asphaltenes, enhancing their thermal stability and structural integrity for the subsequent high-temperature environments of carbonization.

The overall goals of the subsequent tests are to:

1. Tailor the interlayer spacing of the final hard carbon project so that it can accommodate the large atomic radius of sodium ions (1.02Å),
2. Increase defect ratio and surface area to boost reaction kinetics.

This is to be done so that these hard carbons can serve as suitable materials for future projects involving sodium-ion batteries.

X-ray diffraction (XRD) analysis on the treated SVR2-97 revealed a similar XRD pattern to hard carbons. The presence of hard carbons is significant because it points towards a material with the potential for high sodium-ion intercalation due to its disordered structure, offering a promising avenue for developing efficient energy storage systems.

3.2 Experimental Procedure

Thread Innovations supplied pre-treated asphaltene powder to prepare the asphaltene-derived hard carbons. The powder underwent a two-step grinding process. An initial manual grinding of 5 minutes took place using a mortar and pestle, followed by a 250 µm mesh sieve that was employed to filter out larger particles. In Chapter 4, a grinding time of 10 and 15 minutes was also conducted to see if the differing particle sizes influenced final parameters.

The thermal treatment of the asphaltene powder was conducted in a controlled environment using an MTX OTF-1200X tubular furnace with a quartz tube. 1g of SVR2-97 was evenly distributed in an alumina crucible and exposed to an air atmosphere (maintained at a flow rate of 400 mL min^{-1}). The temperature was gradually increased to 300°C at a rate of 1.5°C/min, with a subsequent holding time of 120 minutes. In Chapter 5, the holding temperature, heating rate and holding time were manipulated. The sample was then allowed to air cool to room temperature.

Post-stabilization, the powder was subjected to a secondary grinding for 5 minutes using a mortar and pestle to separate any particles that may have fused. The samples were then put into a GSL-1700X tube furnace with an alumina tube under a nitrogen atmosphere (flow rate of 50 mL min^{-1}), where an alumina crucible was loaded with roughly 0.25g of each sample. The programming consisted of an initial step involving heating to 60°C at a heating rate of 1.5°C/min and holding for 15 minutes to purge the system of residual air. Subsequently, the material was heated to 1200°C from 60°C at a heating rate of 3°C/min and was maintained at this temperature for 120 minutes. Experiments with other carbonization hold temperatures and heating rates will be discussed in Chapter 6. The sample was then allowed to furnace cool back to room temperature. After the completion of the heat treatments, the carbonized material was manually ground using a mortar and pestle to obtain a fine, homogeneous powder ready for analytical characterization.

The subsequent chapters of this thesis delve into the comprehensive analysis of the treated material, with each section highlighting specific treatment parameters. These chapters elaborate on the controlled variables, detailing their respective adjustments tailored to induce the desired alterations in the asphaltene-derived hard carbons.

3.3 Analysis Methods

3.3.1 X-Ray Diffraction (XRD) Analysis

X-ray diffraction was conducted at the nanoFAB at the University of Alberta. XRD is a non-destructive technique that allows for the identification and characterization of the crystallographic structure of materials. The instrument, operating at 38 kV and 38 mA using a Cu K-alpha radiation source, captured diffraction patterns within a range of 10° to 90° 2Theta, with a step increment of 0.05° and a scan speed of 2°/min. This analysis is critical in determining the phase composition and assessing structural changes post-treatment.

3.3.2 Raman Spectroscopy

Raman spectroscopy was conducted at the nanoFAB at the University of Alberta. Employed to probe the vibrational modes of molecules, Raman spectroscopy, performed with a Renishaw InVia Raman Microscope, provided insights into the structural integrity and disorder within the materials. Parameters included a 532nm laser, a 1200 l/mm grating, an exposure time of 2 seconds, a laser power set at 0.1%, and ten accumulations to obtain the Raman spectrum.

3.3.3 Particle Size Distribution Analysis

Particle size distribution was conducted at the Institute for Oil Sands Innovation (IOSI) lab at the University of Alberta. It is essential for predicting the behaviour of the material in practical applications. This was measured using a Mastersizer 3000, in which the particles are first dispersed in a suitable medium to prevent aggregation. Then the particles pass through a laser, which scatters light at various angles depending on their size. The detectors capture the scattered light and are analyzed to determine the particle size distribution.

3.3.4 Mass Determination

Throughout the experimental process, accurate mass measurements were essential. Using a Mettler Toledo XS 105 balance with a resolution of 0.001 mg, precise mass quantification was utilized for subsequent analyses.

3.3.5 Elemental Analysis (CHNS)

Elemental analysis was conducted at the Institute for Oil Sands Innovation (IOSI) lab at the University of Alberta. To determine the percentage of carbon, hydrogen, nitrogen, and sulfur in the samples, a Thermo Flash 200 Elemental Analyzer was employed. This analysis is critical for evaluating the purity and composition of the carbon-based materials. The samples were prepared in tin capsules and loaded into the autosampler. This tested each tin capsule in an oxidation/reduction reactor heated to 1000^{o}C. The tin capsule undergoes combustion, and the elemental gases go through a detector to determine its carbon, hydrogen, nitrogen, and sulfur content. These results were first calibrated according to 2,5-Bis (5-tert-butyl-benzoxazol-2-yl) thiophene (BBOT) as the standard.

3.4 Formulas and Calculations

Below are the formulas used for material characterization. Please refer to Appendix B for sample calculations and more information.

3.4.1 Oxidation Weight Changes Calculations

Measuring the changes in mass observed after oxidation was important, as it allows for a rough estimate of the extent of oxidation during the process. This is indicated by:

$$\boldsymbol{Diff = \frac{m_f - m_i}{m_i} \times 100} \qquad \textbf{(3.4.1)}$$

Where:

- $\%Diff$ represents the percentage difference between the initial and final values after oxidation and is expressed as a percentage
- m_i refers to the initial mass value of the sample before oxidation
- m_f refers to the final mass value of the sample after oxidation.

3.4.2 Total Yield Calculations

The measurement of the total yield gives a better picture of the effect of the entire process on the final yield post-carbonization. This allows for the determination of the experiment's conversion efficiency and the economic viability of the production process. The formula indicates this process:

$$\boldsymbol{Total\,Yield = \frac{m_{o\_f}}{m_{o\_i}} \times \frac{m_{c\_f}}{m_{c\_i}} \times 100} \qquad \textbf{(3.4.2)}$$

Where:

- Total Yield refers to the percentage of the initial material that has been converted after oxidation and carbonization

- m_{o_f} is the mass of the material after oxidation
- m_{o_i} is the mass of the material before oxidation
- m_{c_i} is the mass of the material put into the crucible before carbonization
- m_{c_f} is the mass of the material after carbonization

3.4.3 D-Spacing Calculation

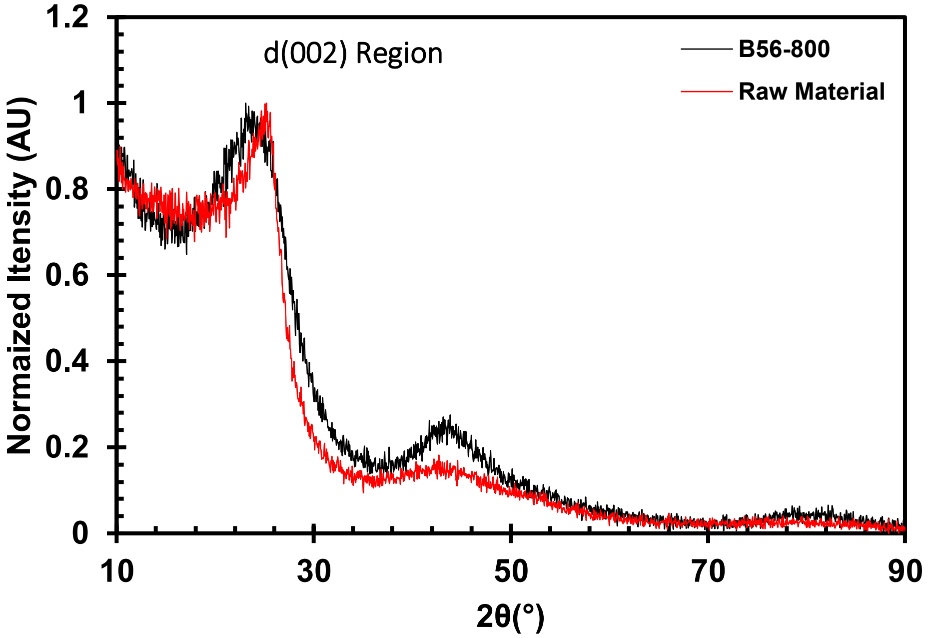

***Figure 4*:** XRD before and after 800°C carbonization for sample oxidized at 300°C for 60 min at a rate of 1.5°C/min

X-ray diffraction was utilized to examine each sample's interplanar spacing and degree of graphitization. Hard carbons have two broad diffraction peaks at 24.8° and 43.8°, as shown in Figure 4. The peak at 24.8° is often associated with graphitic carbon structures, whereas the peak at 43.8° is often related to amorphous/disordered carbons. The regions of interest were only of the 20° – 30° region as they correlate with the distance between graphitic stacking known as the d-spacing. By utilizing a Gaussian regression, as indicated by Figure 5, the d-spacing was calculated by looking at the location of the d(002) peak.

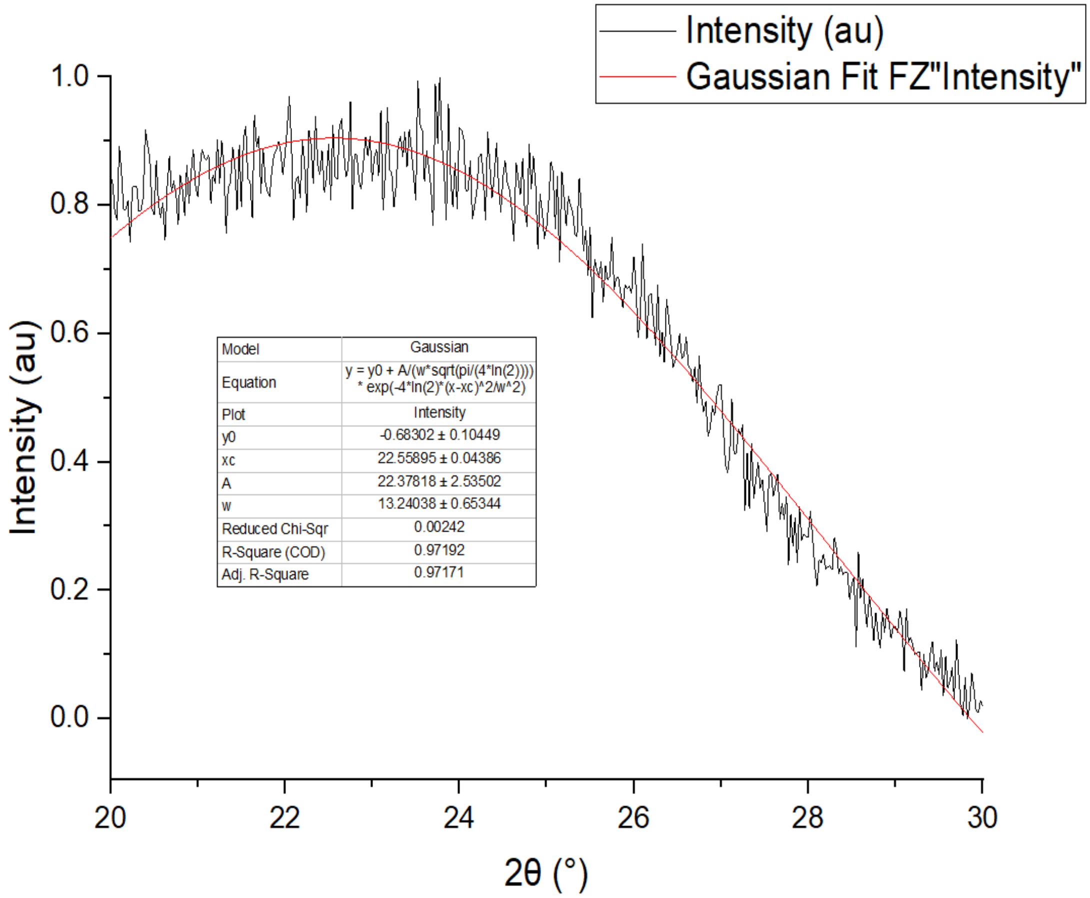

Model	Gaussian
Equation	y = y0 + A/(w*sqrt(pi/(4*ln(2)))) * exp(-4*ln(2)*(x-xc)^2/w^2)
Plot	Intensity
y0	-0.68302 ± 0.10449
xc	22.55895 ± 0.04386
A	22.37818 ± 2.53502
w	13.24038 ± 0.65344
Reduced Chi-Sqr	0.00242
R-Square (COD)	0.97192
Adj. R-Square	0.97171

Figure 5: Gaussian non-linear line fitting

Figure 5 provides an example of what the Gaussian fitting would look like when compared to the XRD spectrum after many iterations.

We then use the Bragg's law equation to calculate for d-spacing:

$$\boldsymbol{d_{(002)} = \frac{\lambda}{2sin\theta}} \qquad \textbf{(3.4.3)}$$

Where:

- $\boldsymbol{d_{(002)}}$ is the interplanar spacing corresponding to the 002 direction in angstroms, which is located in the broad peak located in the 24.8° region for the 2θ axis in the XRD pattern

- $\boldsymbol{\lambda} = 1.5406\text{Å}$, where it is the wavelength corresponding to the Cu K-alpha source of the XRD
- $\boldsymbol{\theta} = \frac{xc}{2}$, where xc is the value in degrees of the results table that corresponds to the location of the maximum peak value of the band in the 002 direction for the XRD pattern

3.4.4 Elemental Analysis Calculations

3.4.4.1 Elemental Ratios to Carbon

Examining the elemental ratios such as H/C, O/C, N/C, and S/C are critical in characterizing carbon-based materials. The formula used to calculate each of the ratios is indicated below.

$$\frac{X}{C} = \frac{n_X}{n_C} = \frac{m_X}{m_C} \times \frac{M_X}{M_C} \qquad \textbf{(3.4.4.1)}$$

Where:

- $\frac{X}{C}$ refers to the ratio of the number of the targeted element to carbon
- n_X is the mols of the element of interest in the sample
- n_C is the mols of carbon in the sample
- m_X is the mass of the element of interest in the sample
- m_C is the mass of the carbon in the sample
- M_X is the molecular weight of the element of interest
- M_C is the molecular weight of carbon

3.4.4.2 (NOS)/C Ratio

The (NOS)/C ratio combines the changes experienced for each heteroatom and looks at them together. The formula to calculate this ratio is indicated below.

$$\frac{NOS}{C} = \frac{n_N+n_O+n_S}{n_C} = \frac{m_N+m_O+m_S}{m_C} \times \frac{M_N+M_O+M_S}{M_C} \qquad \textbf{(3.3.4.2)}$$

Where:

- $\frac{\boldsymbol{NOS}}{\boldsymbol{C}}$ refers to the ratio of nitrogen, oxygen, and sulfur to carbon, which is the ratio of the sum of nitrogen (N), oxygen (O) and sulfur (S) per carbon (C)
- $\boldsymbol{n_N}$ is the mols of nitrogen in the sample
- $\boldsymbol{n_O}$ is the mols of oxygen in the sample
- $\boldsymbol{n_S}$ is the mols of sulfur in the sample
- $\boldsymbol{n_C}$ is the mols of carbon in the sample
- $\boldsymbol{m_N}$ is the mass of the nitrogen in the sample
- $\boldsymbol{m_O}$ is the mass of the oxygen in the sample
- $\boldsymbol{m_S}$ is the mass of the sulfur in the sample
- $\boldsymbol{m_C}$ is the mass of the carbon in the sample
- $\boldsymbol{M_N}$ is the molecular weight of nitrogen
- $\boldsymbol{M_O}$ is the molecular weight of oxygen
- $\boldsymbol{M_S}$ is the molecular weight of sulfur
- $\boldsymbol{M_C}$ is the molecular weight of carbon

3.4.5 I_D/I_G Ratio Calculations with Raman Spectroscopy

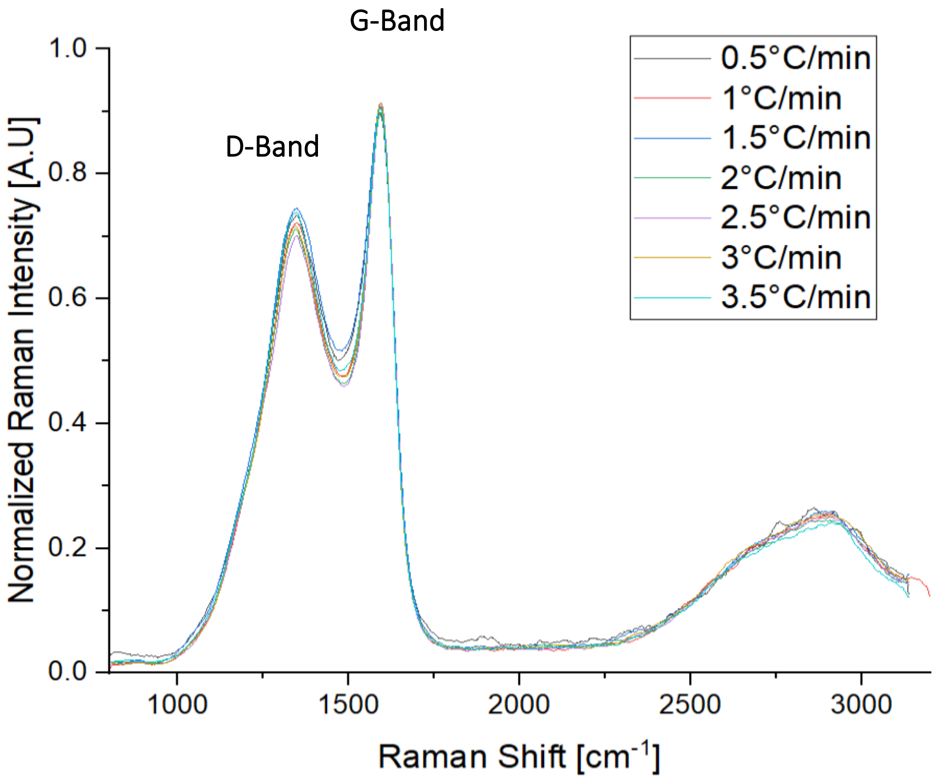

Figure 6: Sample Raman spectrum for different oxidation heating rates at 300°C for 60 min carbonized at 800°C

Two characteristic peaks can be observed in the Raman spectrum for hard carbons. These peaks are located at ~1350 cm-1 (D-Band), which correlates to the disorder and defects, and the peak at ~1580 cm-1 (G-Band) corresponds to the ordered graphitic structure [1]. This can be seen in Figure 7. To estimate the degree of disorder in the material, an estimation can be done by looking at the ratio of intensity for the area under the D-Band and G-Band (I_D/I_G ratio), which was done through a Gaussian line fitting.

$$\boldsymbol{Ratio = \frac{I_D}{I_G}} \qquad \textbf{(3.4.5)}$$

Where:

- Ratio is the ratio of the intensity of the defect band to the intensity of the graphitic band
- $\mathbf{I_D}$ is the area under the curve for the intensity D-band
- $\mathbf{I_G}$ is the area under the curve for the intensity G-band

3.5 XRD Internal Reference and Experimental Errors

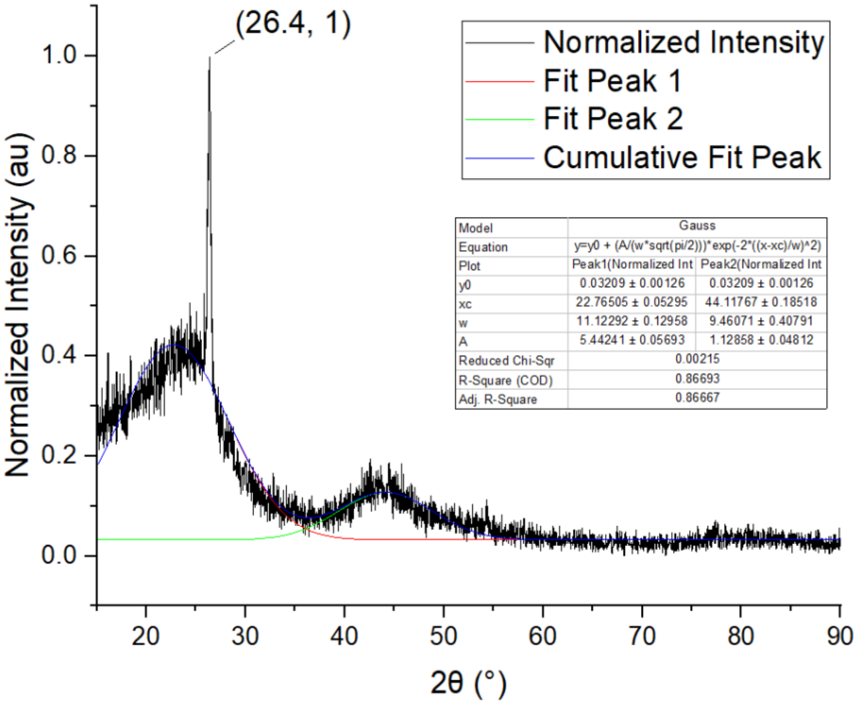

Model	Gauss	
Equation	y=y0 + (A/(w*sqrt(pi/2)))*exp(-2*((x-xc)/w)^2)	
Plot	Peak1(Normalized Int	Peak2(Normalized Int
y0	0.03209 ± 0.00126	0.03209 ± 0.00126
xc	22.76505 ± 0.05295	44.11767 ± 0.18518
w	11.12292 ± 0.12958	9.46071 ± 0.40791
A	5.44241 ± 0.05693	1.12858 ± 0.04812
Reduced Chi-Sqr	0.00215	
R-Square (COD)	0.86693	
Adj. R-Square	0.86667	

Figure 7: XRD Pattern of B56-4 with an internal reference

This set of experiments was utilized to identify if any trends could be observed for a broad range of experimental parameters, primarily focusing on the d-spacing and defect ratios. Figure 7 demonstrates a measurement with an internal reference to see how different the measurements would be by the day compared to conventional graphite. Figure 7 shows that the peak for the internal measurement of graphite corresponds to a d-spacing of 0.337 nm, which differs from the measurement of 0.336 nm of perfect graphite crystals. When comparing XRD results of B56-4 from two different scans, there was also a deviation observed from 0.390nm to 0.393nm. This means that with subsequent scans, there may be machine errors that could affect the results. As tiny variations can equate to a significant difference in d-spacing, it is required to note that these experiments only demonstrate that there can be a potential trend. Still, additional and more refined techniques must be implemented to find the relationship more accurately.

3.6 References

[1] P.-Y. Zhao, J.-J. Tang, and C. Wang, “A low-cost attempt to improve electrochemical performances of pitch-based hard carbon anodes in lithium-ion batteries by oxidative stabilization,” *Journal of Solid State Electrochemistry*, vol. 21, no. 2, pp. 555–562, Sep. 2016, doi: https://doi.org/10.1007/s10008-016-3406-1.

Chapter 4 – Effect of Particle Sizes

4.1 Introduction

Initial experimentation revealed significant variations and discrepancies in results from final analyses, which led to the deduction that they may be due to a wide distribution in particle size. It is hypothesized that smaller particles, with their larger surface area in relation to their volume, are predisposed to a more complete oxidation than larger particles.

Addressing these disparities and promoting uniformity in oxidation across the samples proved necessary to introduce a refinement process to narrow down the range of particle size distributions. Adjusting the grinding protocol was critical in securing a more consistent particle size distribution.

Concurrently, this led to exploring the relationship between particle size and resulting interplanar spacing or d-spacing under uniform treatment conditions at all stages. This investigation was particularly insightful, as it permitted the approximation of the optimal particle size that could yield the most advantageous d-spacing for the given heat treatment parameters.

This section of the study focuses on the impact of varying average particle size on the resultant d-spacing while maintaining constant heat treatment conditions to isolate the effects. The asphaltenes underwent the experimental procedure indicated in Chapter 3.2 to achieve this. The insights gained are utilized to advance our understanding of the material's characteristics.

4.2 Results

4.2.1 Particle Sizes

To get a particle size corresponding to the grinding time for the sample, each sample was analyzed using the Mastersizer 3000 and its results are indicated below in Table 2. Increasing grinding time has resulted in a significant reduction in average particle size.

Table 2: Differing grind times

Sample ID	Test Parameters	
	Grinding Time (min)	**Average Particle Size (µm)**
B56	5	53.7
B57	10	26.1
B58	15	10.7

4.2.2 Mass Changes from Oxidative Stabilization and Carbonization

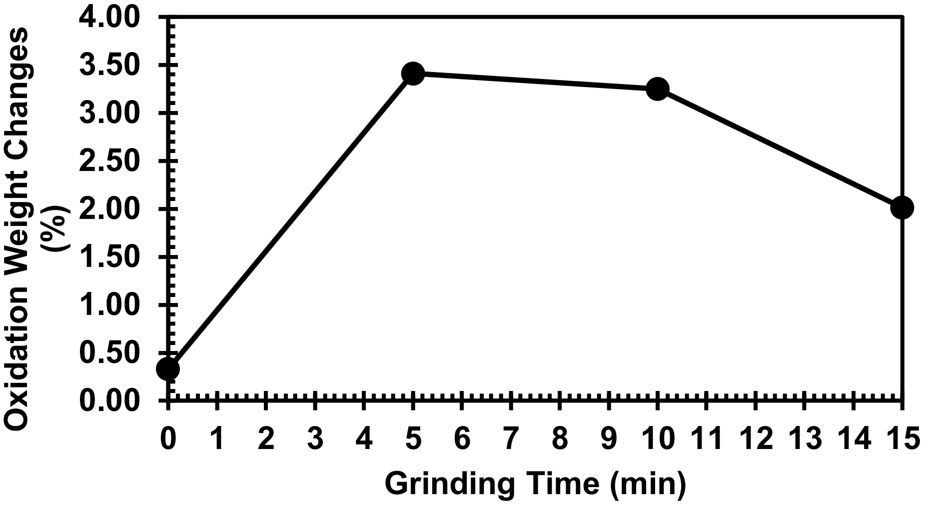

Figure 8: Oxidation weight changes for different grinding times at 300°C for 60 min

Figure 8 presents the impact of grinding time on the oxidative weight changes for the asphaltene samples. The weight increase is caused by the reaction and incorporation of oxygen with the raw material. Initially, the unground sample exhibits a negligible weight gain, which indicates a low degree of oxidation. This is most likely because of insufficient time for oxygen to diffuse toward the core of the large sizes of raw materials. As the grinding time increases to 5 minutes, evidence of a more pronounced increase in weight is observed as the weight gained after oxidation increases from 0.5 wt% to 3.5 wt%. This suggests greater oxidation that could be due to the increased exposure from the surface area and the reach of oxygen to the core of the powders of the raw materials. However, further grinding beyond this point leads to a gradual decline in weight gain that could be caused by the increased materials being over-oxidized. Over-oxidation leads to the conversion of carbon to CO_2. This trend shown in Figure 8 suggests that there may be an optimal grinding time for oxidation.

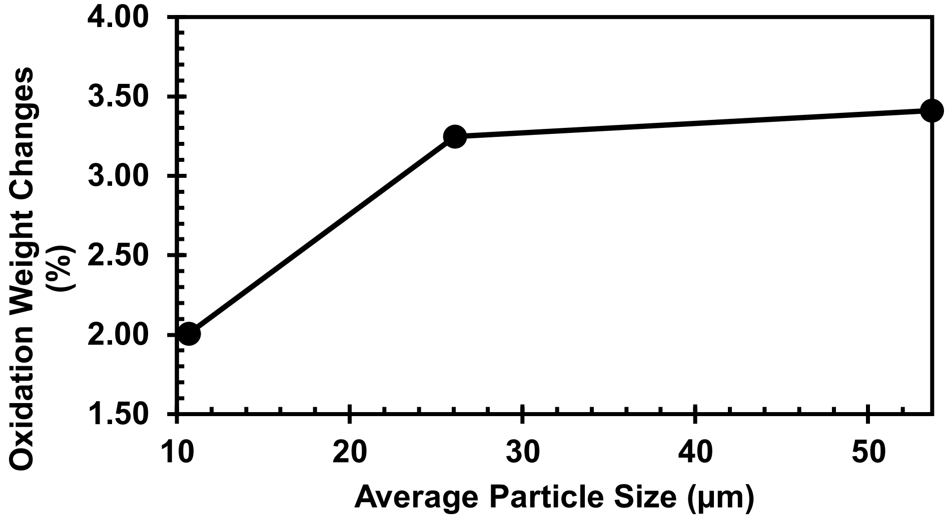

Figure 9: Oxidation weight changes for different average particle sizes at 300°C for 60 min

Figure 9 demonstrates the relationship between the average particle size of the asphaltenes and the corresponding weight changes after oxidation at 300°C for 60 minutes. It can be seen that there is a positive relationship where the oxidation weight gain increases with the corresponding average particle size. This indicates that there is potentially a threshold in particle size between the weight so that there is no longer a capacity for oxidation, leading to no further weight gain. The largest particle size appears to reach an oxidative saturation point, implying a maximum amount of oxygen can be absorbed given the experimental conditions.

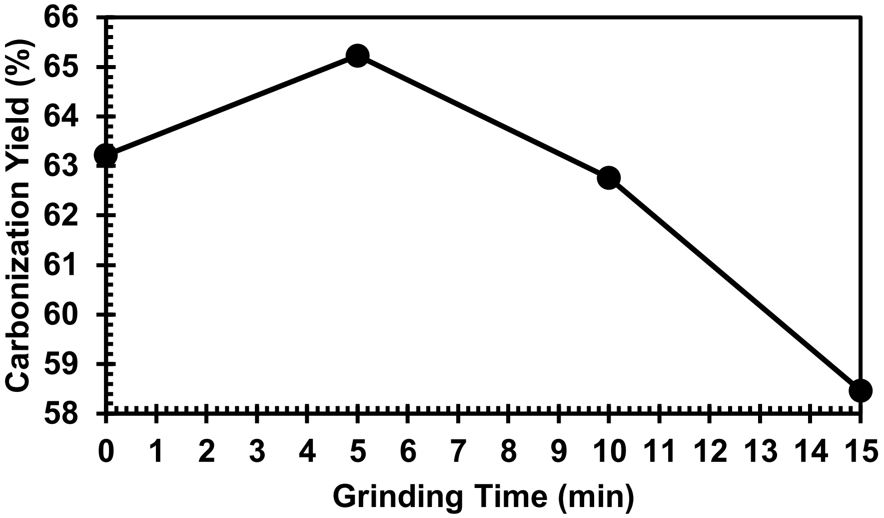

Figure 10: Carbonization yield for different grinding times at 1200°C for 120 min

Figure 10 depicts the effect of grinding time on the yield after carbonization at 1200°C for 120 minutes. All the materials were oxidized at 300°C for 60 min at a heating rate of 1.5°C/min before carbonization. The carbonization yield is the percentage of the final product obtained post-carbonization relative to the initial mass of asphaltene before oxidation. The data exhibits a parabolic trend across the different grinding times. Initially, with no grinding, the yield escalates to a peak at a grinding time of 5 minutes, which signifies the optimal grinding time for maximal yield. Beyond this point, there is a decrease in the yield with increasing grinding time. This suggests that excessive grinding may be detrimental to the carbonization yield.

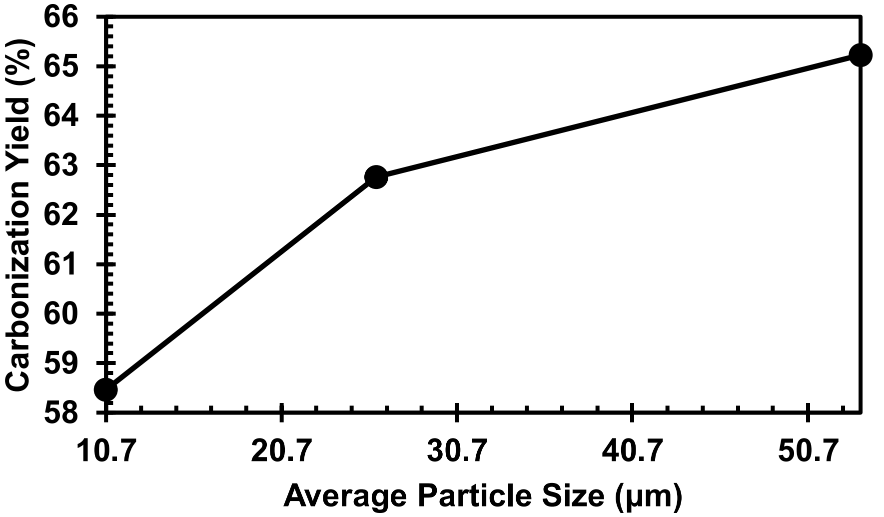

Figure 11: Carbonization Yield for Different Average Particle Sizes at 1200°C for 120 min

Figure 11 illustrates a positive correlation between the average particle size and carbonization yield at a carbonization temperature of 1200°C over a hold time of 120 minutes. The carbonization yield can be seen to increase alongside the particle size. Smaller particles corresponded to lower yields, while the larger particles resulted in significantly higher yields. This suggests that the particle size is a critical factor in the treatment process.

4.2.3 Interplanar Spacing with XRD

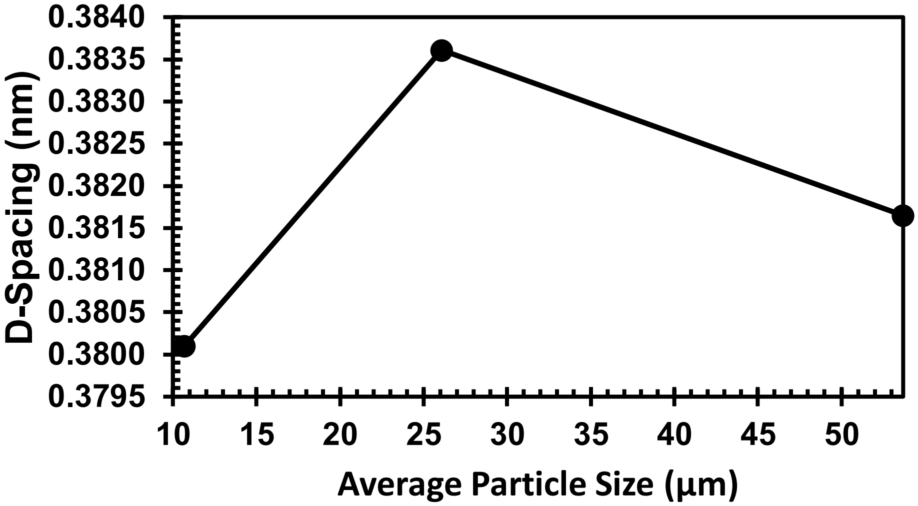

Figure 12: D-Spacing for different average particle sizes at 300°C for 60 min at 1.5°C/min

Figure 12 plots the variation in interlayer spacing (d-spacing) of the carbonized asphaltenes against the average particle size of the sample treated at 300°C for 60 minutes with a rate of 1.5°C/min, which is then carbonized at 1200°C for 120 minutes at a rate of 3°C/min. The data initially exhibits an increase in d-spacing as the particle size enlarges until it reaches a peak within the 25-30 µm range. This peak suggests that there is an optimal particle size to maximize the d-spacing for the given treatment. Following this peak, there is a noticeable reduction in d-spacing with further increases in the particle size. The data may indicate that a specific particle size range may favour the expansion of interlayer spaces in the hard carbon structure.

4.3.4 Elemental Composition

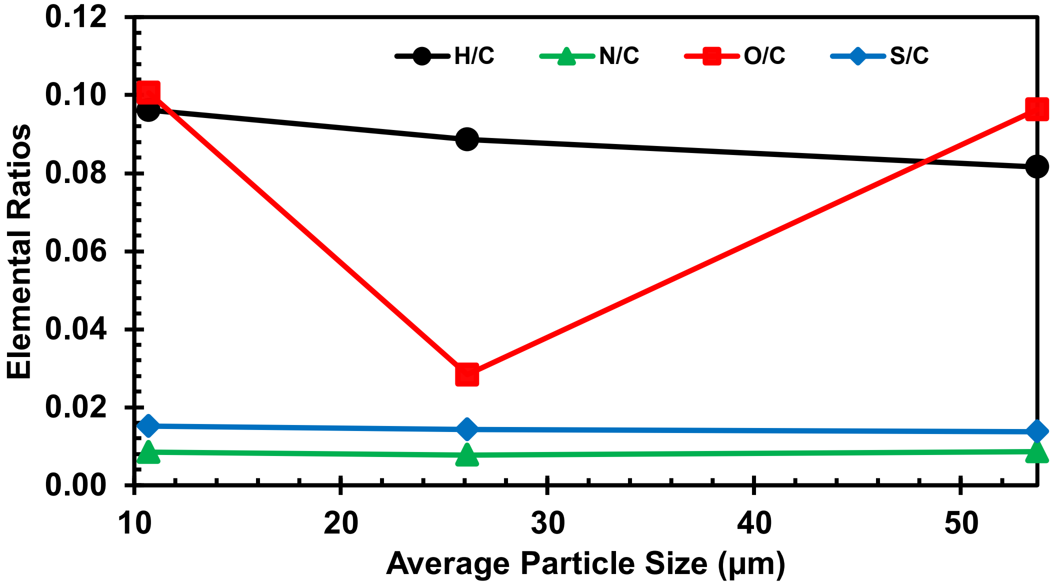

Figure 13: Elemental ratios to carbon after carbonization for differing particle sizes

Figure 13 presents the elemental ratios to carbon, determined by CHNS analysis, after the carbonization of asphaltenes with varying particle sizes. The graph reveals a distinct negative linear trend for the hydrogen-to-carbon (H/C) ratio, which decreases as the particle size increases. This suggests that the larger particle sizes facilitate the loss of hydrogen in a rearrangement of carbon structure, which leads to a lower H/C ratio.

In contrast, the nitrogen-to-carbon (N/C) and sulfur-to-carbon (S/C) ratios remain relatively constant across the whole range of particle sizes tested. This implies that the particle size does not significantly impact the nitrogen and sulfur content within the hard carbon for the given oxidation and carbonization conditions.

There is no distinguishable relationship between the O/C ratio and particle size. The smallest and largest particle sizes show the minimal variation that hovers around a ratio of 0.1, a significant drop in the O/C ratio at 22.1 µm. There could be errors in this data that could account for this drop at this point and may not be indicative of the true trend.

4.2.5 Raman Spectroscopy

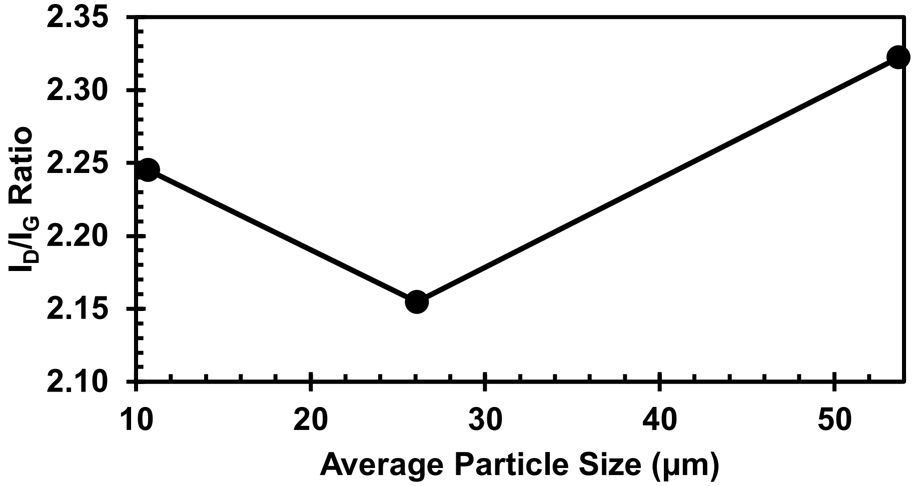

Figure 14: I_D/I_G ratio for varying particle sizes

Figure 14 displays the ratio of the D-band to the G-band intensities (I_D/I_G) obtained from Raman spectroscopy. This ratio indicates the relative order within the carbon lattice, with a higher ratio suggesting greater structural defects. There is no distinguishable trend, but it is observed that the I_D/I_G ratio decreases with increasing particle size up to its minimum at a particle size of 22.1 μm. This indicates the lowest level of defects for the given data. As the particle size increases from this point, the I_D/I_G ratio also increases. Like the previous point for the O/C data, this minimum may be due to errors and may not represent the true trend.

4.3 Discussion

When looking at the data, the particle size does indicate an influence on the weight changes seen during this process. As hypothesized in Section 4.1, this would primarily be due to the differing surface areas for each particle size and the distance and time of oxygen diffusion to the core of the particles. Firstly, a smaller particle size will have greater surface area to volume ratio, allowing for more oxygen adsorption sites and diffusion into the material. Secondly, a smaller radius for the particle will allow for a shorter distance for oxygen to diffuse through the particle, resulting in more complete oxidation. When looking at the larger particle sizes, the surface area to volume ratio is reduced, lessening the amount of oxygen that can be diffused into the particle at a time. However, in the case of these experiments, it is believed that for the given conditions the particles are undergoing, there will always be sufficient time for oxygen to be absorbed into them. Therefore, a larger particle size (corresponding to certain treatment conditions) allows for the most significant weight gain as it has a greater volume, leading to having the most room to accommodate oxygen, as illustrated in Figure 8. Figures 10 and 11 show that the highest yield following carbonization follows a similar trend to the observed oxidation weight changes. Similar to the oxidation step, the larger surface area and smaller diffusion distance due to the smaller radii of the smaller particles enable a more efficient escape of gases and impurities during carbonization. Additionally, reduced weight gain for smaller particles could be due to over-oxidation as more carbon reacts with oxygen to produce CO_2 gas released to the environment. This process results in a lower final product yield for smaller particle sizes. In general, the smaller the sample, the greater the weight loss, as the primary decomposition particles are less susceptible to secondary reactions as they diffuse through a smaller sample, which would result in a more significant weight loss noted when smaller samples are degraded under an inert atmosphere [3]. This process results in a lower final product yield for smaller particle sizes. Similar findings were found in coke yield, as it was found that the coke yield during carbonization is dependent on the ratio of total volume to surface area, indicating that this is a diffusion-driven process.[4].

While some fluctuations are seen in the O/C ratio for the particle size corresponding to 26.1 μm, the change can be from the estimation of oxygen from the CHNS test. However, it is observed that there is a relatively linear trend in particle size and the H/C ratio. The H/C ratio decreases as particle size increases, indicating a greater degree of graphitization.

The Raman spectroscopy results indicate that the defect ratio is minimized at 22 μm but then maximized at 57.1 μm. Previous studies have shown that particle sizes in biomass can affect the pyrolysis process. Zhou et al. believed that a larger particle size could increase the total gas production and carbon conversion efficiency [1], which is also observed in these samples. It is also mentioned that precursors with larger particle sizes present a faster reaction rate and a more volatile release rate during the pyrolysis process, which is conducive to forming additional pore structures and defects [2]. Low-cost and high yield are desperately wanted for hard-carbon materials as current precursors have high cost and low yield [5]. The larger particle size was chosen, providing the highest yield while maintaining a relatively high d-spacing.

4.4 Conclusions

The experimental investigations reveal particle size's crucial role in the oxidative stabilization and carbonization processes. We found that particle sizes can influence the material's behaviour during heat treatments. Larger particles were shown to have increased weight gain during oxidative stabilization compared to smaller particles, suggesting they can accommodate a higher oxygen concentration. Similarly, these larger particles provided higher yields during carbonization, indicating that particle size directly affects carbonization efficiency. The XRD established that the maximum interplanar spacing observed in this experiment is associated with a particle size of 26.1 μm under oxidation conditions of 300°C at a heating rate of 1.5°C/min held for 120 min followed by carbonization conditions of 1200°C at a heating rate of 3°C/min held for 120 min. Additionally, a decrease in the H/C ratio with larger particle sizes hints at increased graphitic structure, likely due to more effective heat transfer within the larger particles. In essence, this study reveals the importance of particle size in optimizing heat treatment processes for carbonaceous materials, laying the groundwork for refining production techniques to enhance the properties of carbon materials for energy storage and other applications.

4.5 References

[1] T. Zhou, S. Yang, Y. Wei, J. Hu, and H. Wang, "Impact of wide particle size distribution on the gasification performance of biomass in a bubbling fluidized bed gasifier," vol. 148, pp. 534–547, Apr. 2020, doi: https://doi.org/10.1016/j.renene.2019.10.059.

[2] Y. Niu, H. Tan, Y. Liu, X. Wang, and T. Xu, "The Effect of Particle Size and Heating Rate on Pyrolysis of Waste Capsicum Stalks Biomass," *Energy Sources, Part A: Recovery, Utilization, and Environmental Effects*, vol. 35, no. 17, pp. 1663–1669, Sep. 2013, doi: https://doi.org/10.1080/15567036.2010.509084.

[3] J. Drbohlav and W. T. K. Stevenson, "The oxidative stabilization and carbonization of a synthetic mesophase pitch, part II: The carbonization process," *Carbon*, vol. 33, no. 5, pp. 713–731, 1995, doi: https://doi.org/10.1016/0008-6223(95)00012-3.

[4] H. Marsh, In Introduction to Carbon Science (Edited by H. Marsh), Chapter 3. Butterworths, London (1989).

[5] P.-Y. Zhao, J.-J. Tang, and C. Wang, "A low-cost attempt to improve electrochemical performances of pitch-based hard carbon anodes in lithium-ion batteries by oxidative stabilization," *Journal of Solid State Electrochemistry*, vol. 21, no. 2, pp. 555–562, Sep. 2016, doi: https://doi.org/10.1007/s10008-016-3406-1.

Chapter 5 – Modification of Oxidation/Stabilization Parameters

5.1 Introduction

This section will focus on exploring d-spacing through optimization of oxidative stabilization parameters. An oxidative stabilization step is necessary to convert asphaltenes to hard carbon structures due to their low softening point, leading to melting under carbonization temperatures ranging from 800-1500°C. During carbonization, it is known that the aromatic condensation of polycyclic aromatic constituents occurs primarily at temperatures ranging between 400-500°C, which results in a highly ordered carbonaceous mesophase, which is an intermediate to highly graphitic carbons [1]. It is hypothesized that aromatic condensation can be avoided by introducing oxygen as carbonyl functionalities during oxidation [1]. This method preserves the asphaltenes' inherent turbostratic structure by impeding the graphitic sheet alignment that would otherwise form during carbonization. The oxidative stabilization process inhibits particle fusion, making the material less prone to thermal degradation during carbonization. Which ultimately results in the formation of hard carbons.

Although the application of oxidative stabilization in creating asphaltene-derived carbon fibres and other precursors has been explored, it has yet to be examined for producing asphaltene-derived hard carbons. Although not completely understood in asphaltenes, the underlying oxidation mechanisms are believed to be vital for the successful development of these hard carbon materials.

This research utilizes the oxidative stabilization step to introduce varying degrees of d-spacing and structural defects within the asphaltene-derived hard carbons by introducing oxygen within the material. These modifications could enhance sodium-ion intercalation and electrical conductivity, thus elevating the performance of SIBs.

5.2 Experimental Procedure

The experiment followed the procedure outlined in Chapter 3 for the oxidative stabilization and carbonization process. The experimental methodology was altered slightly with these separate conditions:

1. **Oxidation Temperature:** This set of experiments examined a temperature bracket of 275°C to 325°C, increasing in 25°C intervals.

2. **Holding Time:** Oxidative durations spanned from 30 to 90 minutes, extended in 30-minute increments.

3. **Heating Rate:** The heating rate was adjusted from 0.5°C/min to 3.5°C/min in 0.5°C/min increments.

By examining these parameters, this chapter intends to refine the stabilization process to increase the understanding of asphaltene behaviour under oxidative conditions and to increase energy storage capabilities.

The oxidation/stabilization experiments followed the parameters indicated in Table 3 and were conducted utilizing asphaltenes with a particle size of 53.7 µm.

Table 3: Oxidative stabilization treatment conditions

Temperature (^oC)	Holding Time (min)	Heating Rate (^oC/min)
275	30	0.5
300	60	1
325	90	1.5
		2
		2.5
		3
		3.5

5.3 Results

5.3.1 Mass gain/loss during Oxidation & Carbonization

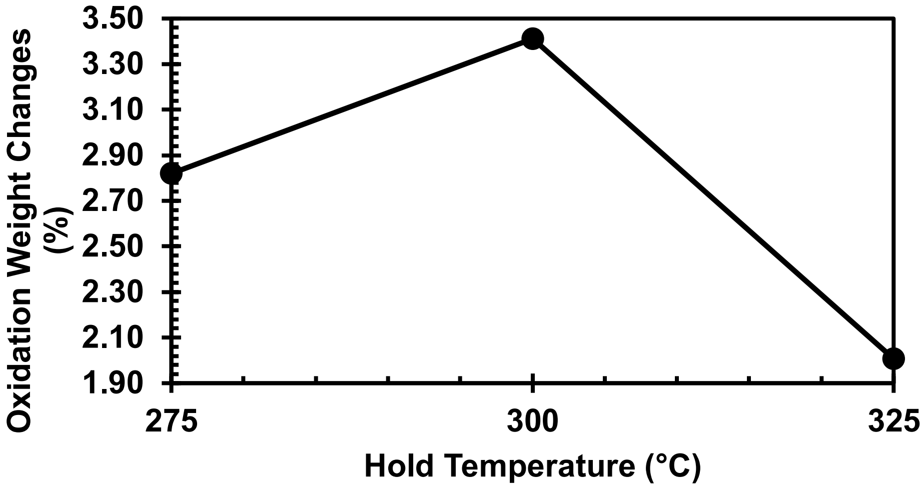

Figure 15: Oxidation weight changes for different oxidation holding temperatures for 60 min at a heating rate of 1.5°C/min

Figure 15 illustrates the effect of various holding temperatures on the weight changes observed during oxidation. The data demonstrates that the weight changes increase with temperature and peak at 300°C. However, when the temperature rises beyond 300°C, there is a decrease in weight change. This trend demonstrates the sensitivity of the d-spacing to oxidation temperature and that identifying the optimal holding temperature is essential to producing asphaltene-derived hard carbons.

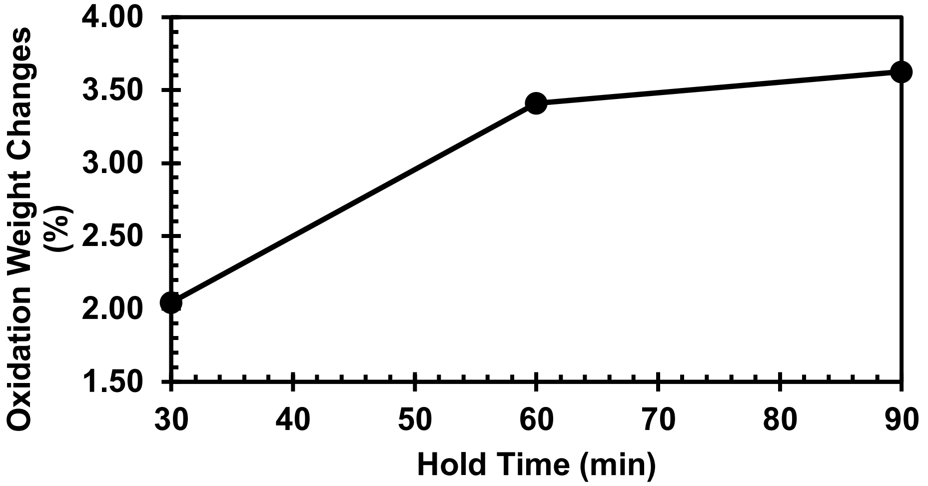

Figure 16: Oxidation weight changes for different oxidation hold times at 300°C and a heating rate of 1.5°C/min

Figure 16 presents the relationship between the oxidation hold time and the resultant changes in sample weight. The data shows that the weight changes steadily increase from 30-60 minutes, indicating a relatively stable oxidation process. After 60 minutes, the data levels off, suggesting that the weight gain due to oxidation stabilizes and a plateau is reached.

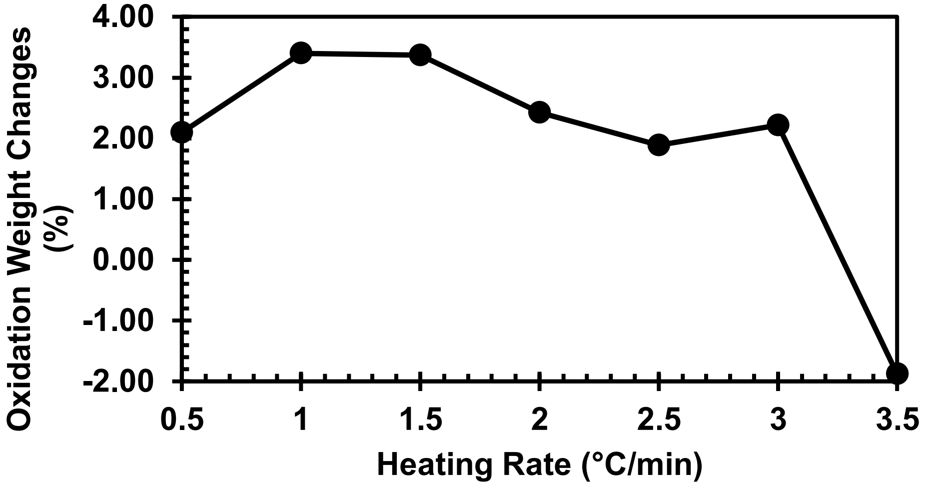

Figure 17: Oxidation weight changes for different oxidation heating rates at 300°C for 60 min

Figure 17 explores the effect of varying heating rates on the oxidation-induced weight changes of the asphaltenes. The data shows that there is little change to the observed weight changes until the heating rate exceeds 3°C/min, where this is a notable decline in weight gain, which results in a net weight loss at 3.5°C/min. While it is difficult to see many changes, it can be observed that there may be maximum points corresponding to a region between 1-1.5°C/min. This suggests that there may be a slight effect of heating rate on oxidative weight gain, but once past the threshold of 3°C/min, the weight changes will drastically decrease and even result in weight loss.

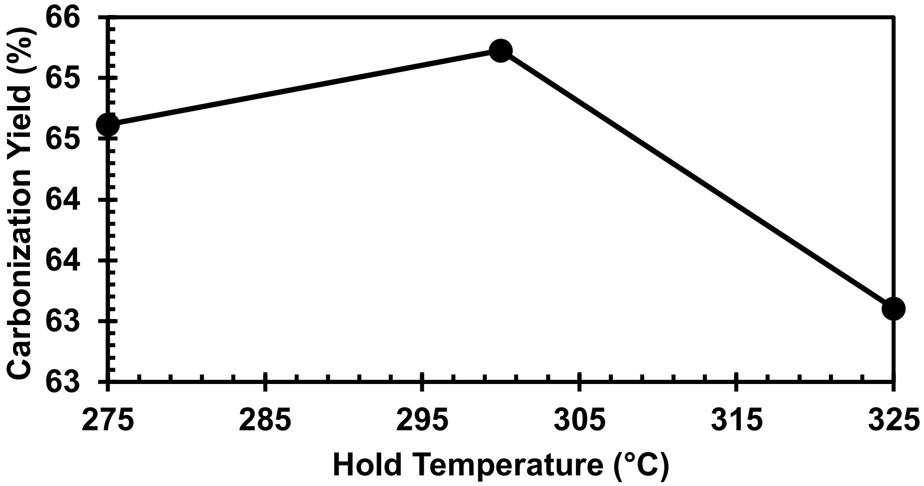

Figure 18: Yield for different oxidation holding temperatures

Figure 18 illustrates the carbonization yield as a function of the oxidation hold temperature. The yield increases with temperature to a maximum of around 300°C. This is followed by a decreasing carbonization yield as the hold temperature increases.

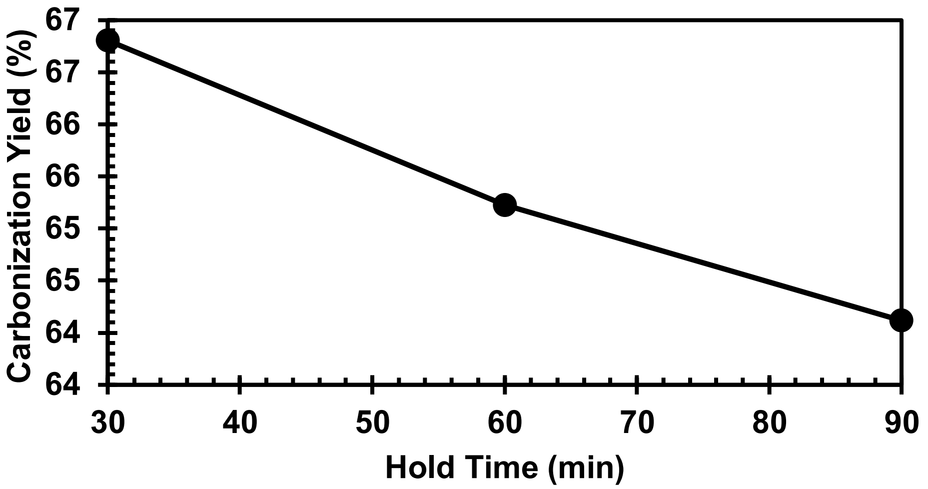

Figure 19: Yield for different oxidation hold times

Figure 19 depicts a negative trend between the carbonization yield and the hold time. The yield starts relatively high and steadily decreases as the hold time increases.

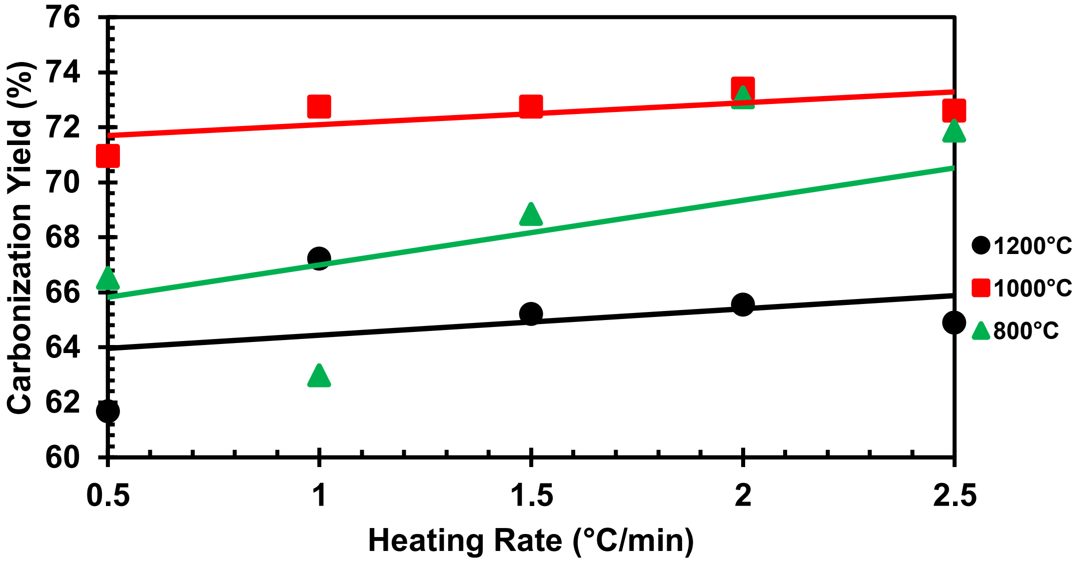

Figure 20: Yield for different oxidation heating rates

Figure 20 shows the effect of the heating rate on the carbonization yield for each different carbonization temperature. The data generally increases as the heating rate increases for both the

1000°C and 1200°C samples. When looking at the 800°C data, it can be seen that it is difficult to find a trend, but the carbonization yield seems to increase as the heating rate increases.

5.3.2 Interplanar Spacing – XRD Analysis

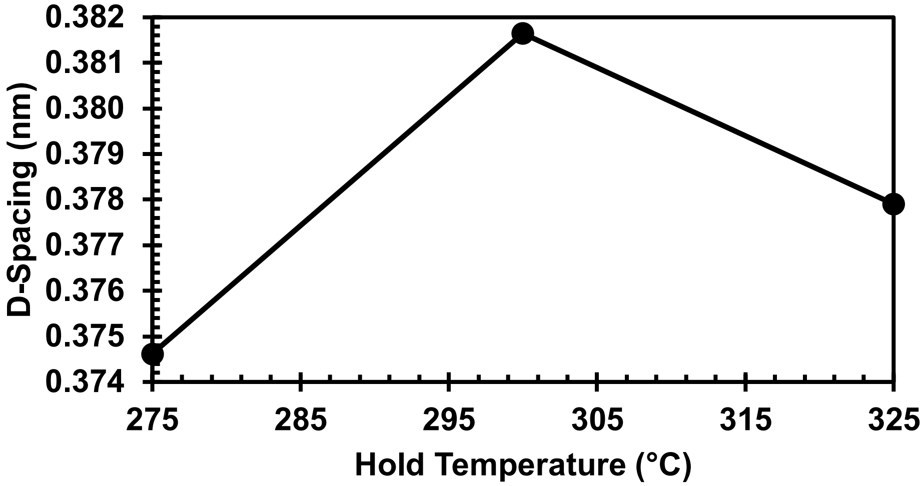

Figure 21: D-Spacing for different holding temperatures carbonized at 800°C for 120 min at a rate of 3°C/min

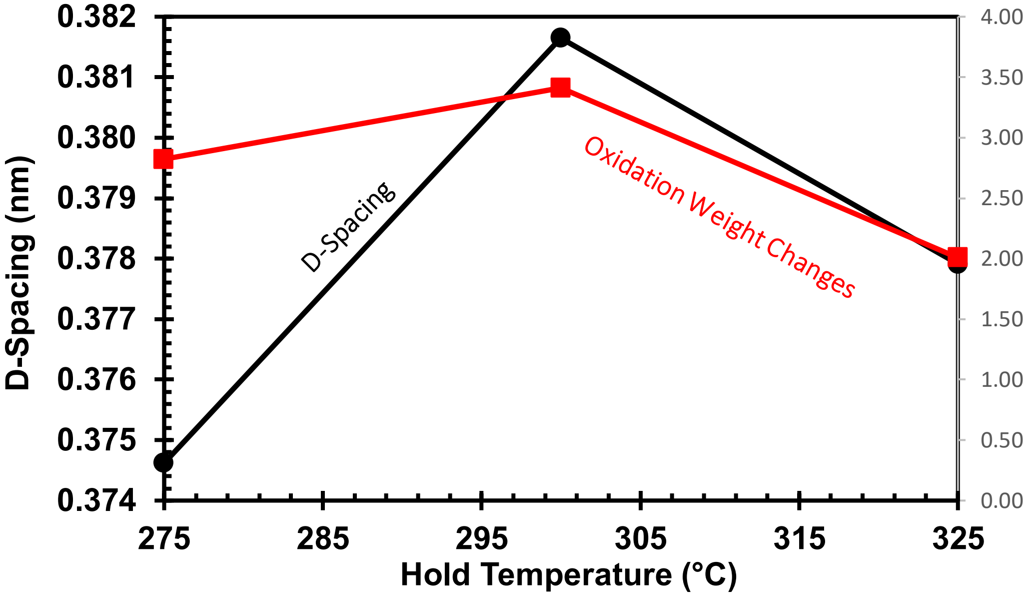

Figure 22: D-Spacing for holding temperatures compared to oxidation weight gains

Figure 21 demonstrates the change of d-spacing with oxidation hold temperature. The d-spacing increases with increasing hold temperature until a maximum is observed at 300°C. A decrease follows this in d-spacing as the hold temperature increases. This suggests that the hold temperature impacts the resultant d-spacing. Given the oxidation conditions of a heating rate of 1.5°C/min and a holding time of 60 min, a hold temperature of 300°C may be optimal to achieve the highest d-spacing.

When observing the d-spacing in relation to oxidation weight changes observed in Figure 22, they mirror similar trends, and the maximum observed positive weight change is observed at the highest d-spacing. This suggests that there may be a correlation between the oxidation weight changes and the d-spacing.

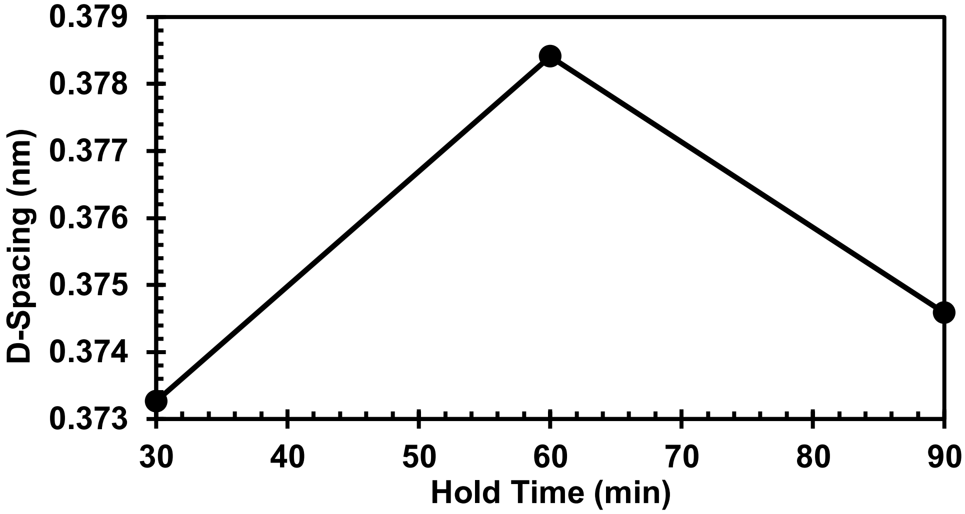

Figure 23: D-Spacing for different holding times carbonized at 800°C for 120 min at a rate of 3°C/min

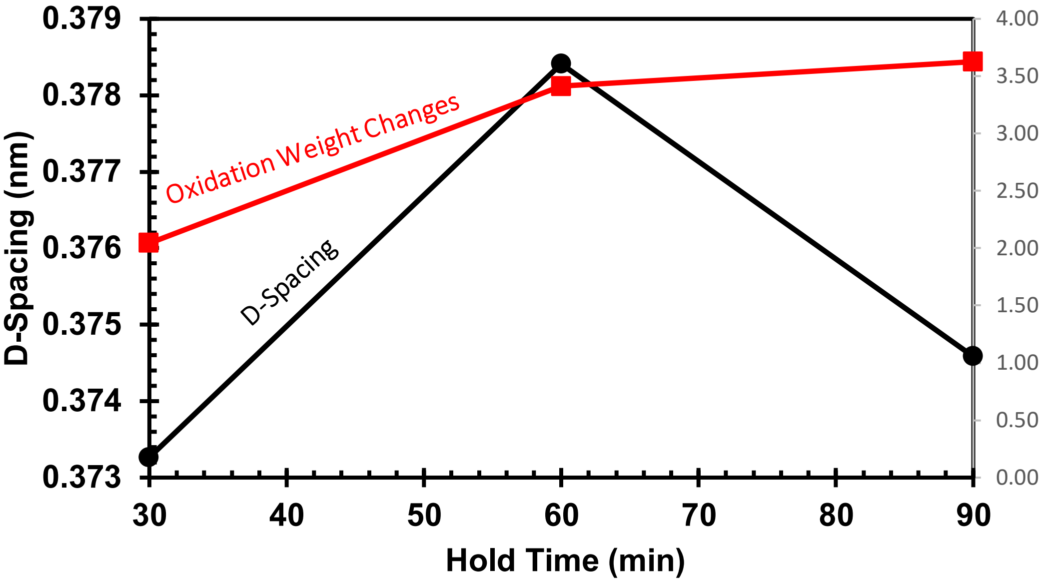

Figure 24: D-Spacing for hold times compared to oxidation weight gains

In Figure 23, the data demonstrates an increase in d-spacing with increased hold time until a hold time of 60 min, where a maximum d-spacing is observed. After the observed maximum, the d-spacing decreases as the hold time increases.

When comparing the data to the oxidation weight change data in Figure 24, the weight change data peaks at a range from 80 to 90 minutes of holding time. This contrasts the peak of the d-spacing observed at a 60-minute hold time. From the comparison of these two results, they exhibit a very weak or little relationship with each other for the varying hold times in the oxidation process.

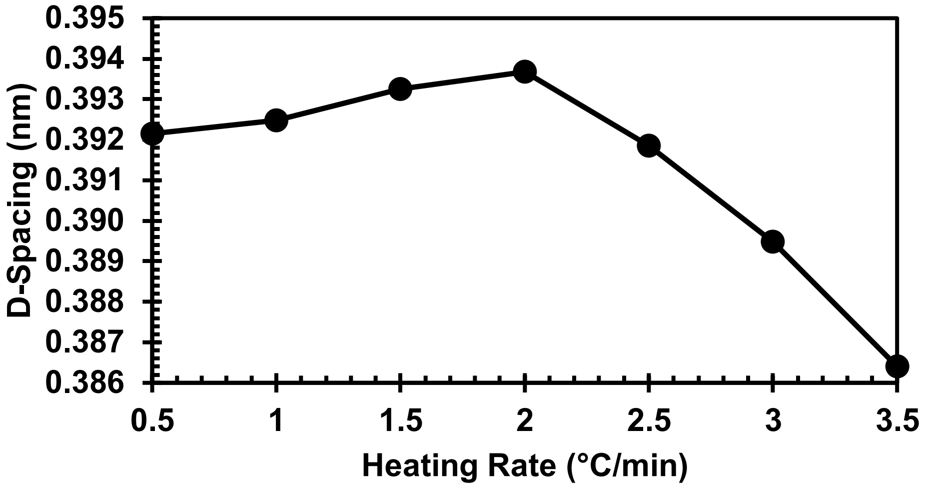

Figure 25: D-Spacing for different oxidation heating rates carbonized at 800°C for 120 min at a rate of 3^{o}C/min

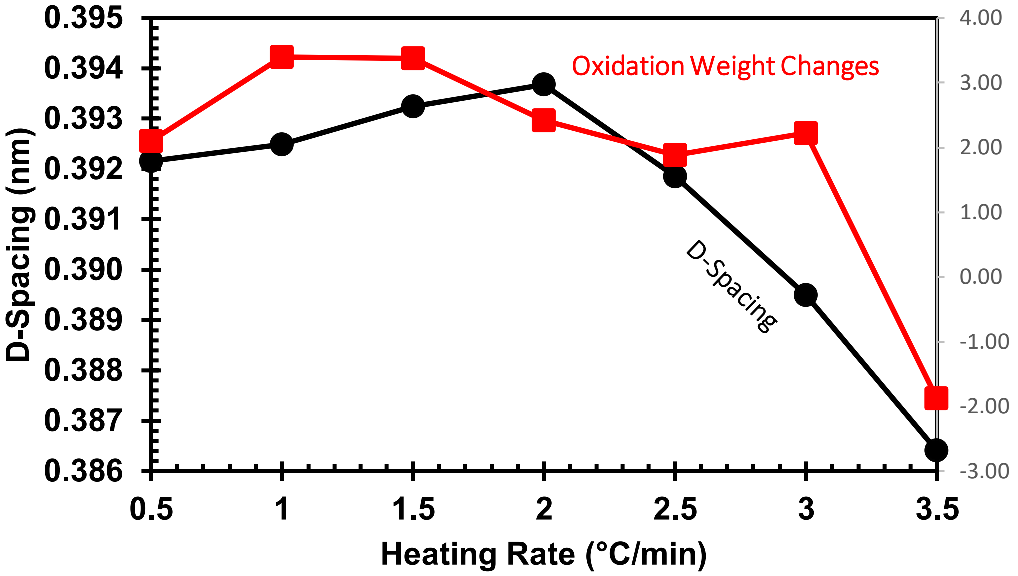

Figure 26: D-Spacing for heating rates compared to oxidation weight gains at a carbonization temperature of 800°C

Figure 25 shows that the d-spacing and heating rate initially increase until they reach an observed maximum of approximately 1.5°C/min. A steady decrease then follows this in d-spacing with increasing heating rate. This indicates an effect on the d-spacing with heating rate and that a maximal value is achieved with a heating rate of 1.5°C/min for the given oxidation conditions of a hold temperature of 300°C and a hold time of 60 minutes.

When comparing the d-spacing data to the oxidation weight changes data in Figure 26, it can be seen that they follow an almost identical trend. This indicates a strong correlation between the oxidation weight changes and the result d-spacing for differing oxidation heating rates.

5.3.3 Elemental Evolution versus Oxidation Parameters

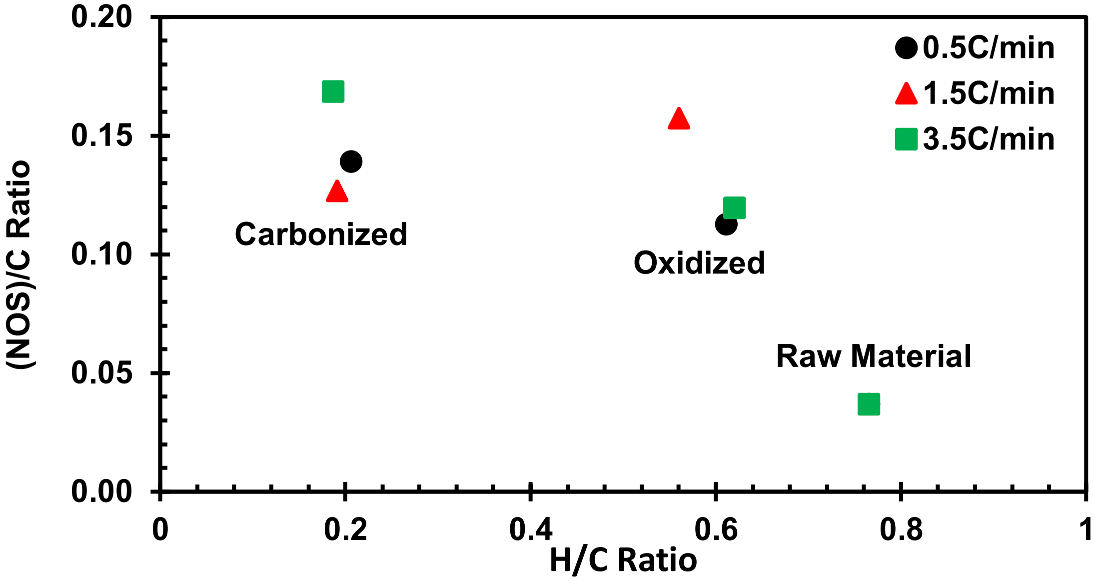

Figure 27: (NOS)/C vs H/C ratio evolution for different oxidation hold temperatures

Figure 27 demonstrates the evolution of the H/C and (NOS)/C ratio after subsequent treatments. The H/C ratio is highest at its raw stage and has the lowest ratio post-carbonization. The (NOS)/C ratio follows the trend of containing the lowest ratio as the raw material but increases throughout different treatment stages. It is noted that the 1.5°C/min sample has a higher (NOS)/C ratio than after carbonization, which contrasts with the samples treated at 0.5°C/min and 3.5°C/min, where the ratio is constantly increasing throughout the treatment stages.

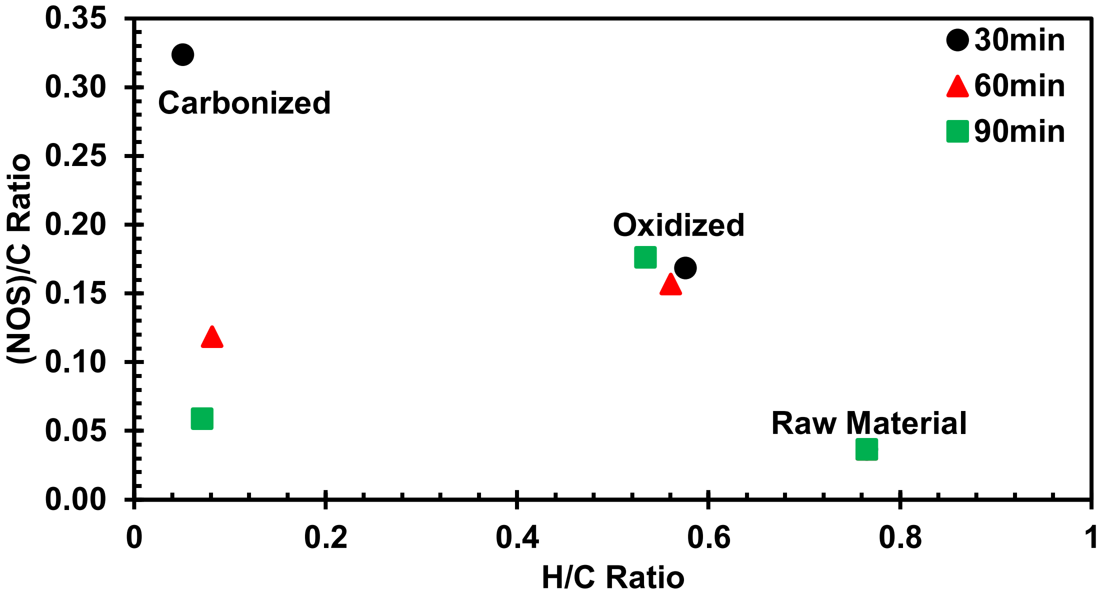

Figure 28: (NOS)/C vs H/C ratio evolution for different oxidation hold time

Figure 28 depicts a H/C ratio that decreases after each treatment stage for all holding times. This begins from its peak as the raw material and ends in a relatively low concentration post-carbonization. It is noted that the (NOS)/C ratio for the 30-minute sample increases for each treatment stage but is shown to decrease after oxidation after reaching its maximum for the other two samples.

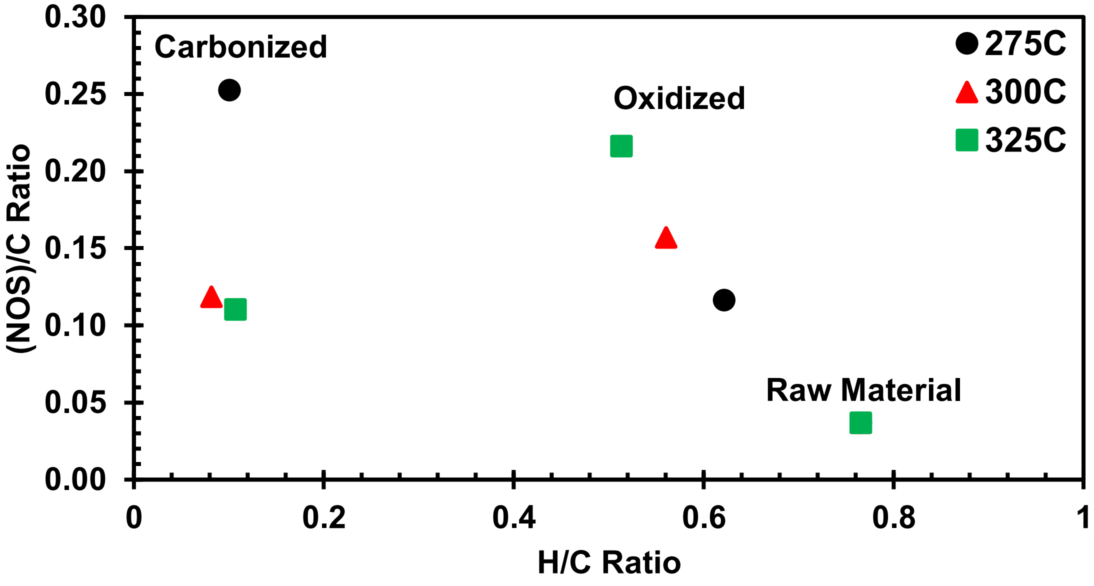

Figure 29: (NOS)/C vs H/C ratio evolution for different oxidation heating rates

Figure 29 demonstrates the same trend for the hold time samples, where the H/C ratio decreases throughout the different treatments. The (NOS)/C ratio peaks during oxidation for the 300°C and 325°C samples and reduces for the subsequent carbonization. The 275°C sample is shown to increase its (NOS)/C throughout each stage of the treatment process.

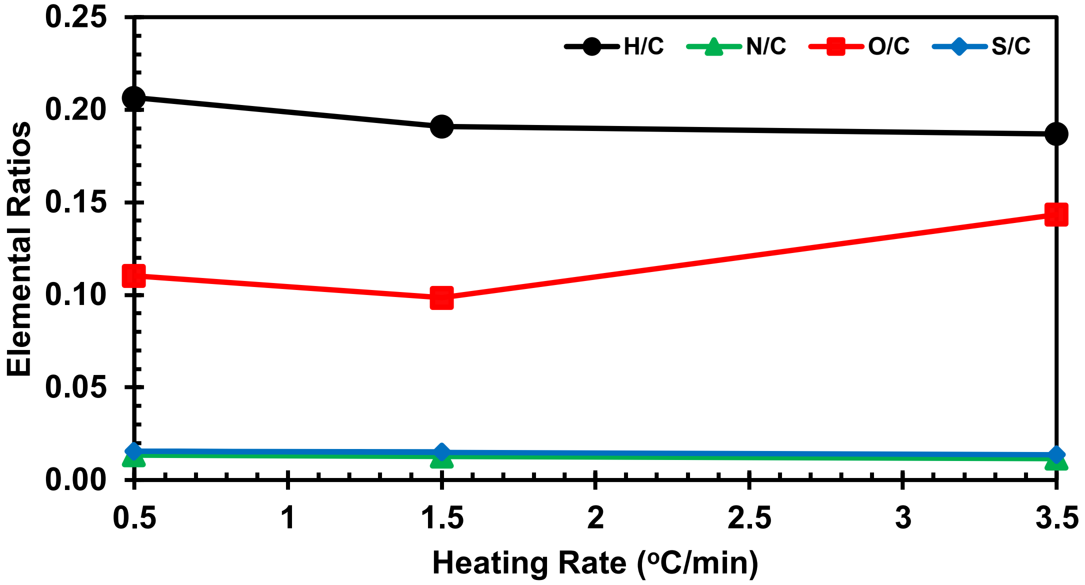

Figure 30: Elemental ratios compared to different oxidation heating rates

According to Figure 30, the heating rate has almost no effect on the nitrogen and sulfur content within the hard carbon. The H/C ratio slightly decreases H as the heating rate increases. It is important to note that the changes in the H/C ratio are relatively small, so the heating rate may not significantly impact the H/C ratio of the resultant hard carbon. The O/C ratio follows a positive trend where the O/C ratio increases for increasing heating rate. It is also important to note that the heating rate tests were carbonized at a lower carbonization temperature of 800°C, significantly lower than the carbonization temperature of the hold time and hold temperature tests, which were conducted at a carbonization temperature of 1200°C. This is why the H/C content is much higher than the other tests and potentially why the O/C ratio is much lower.

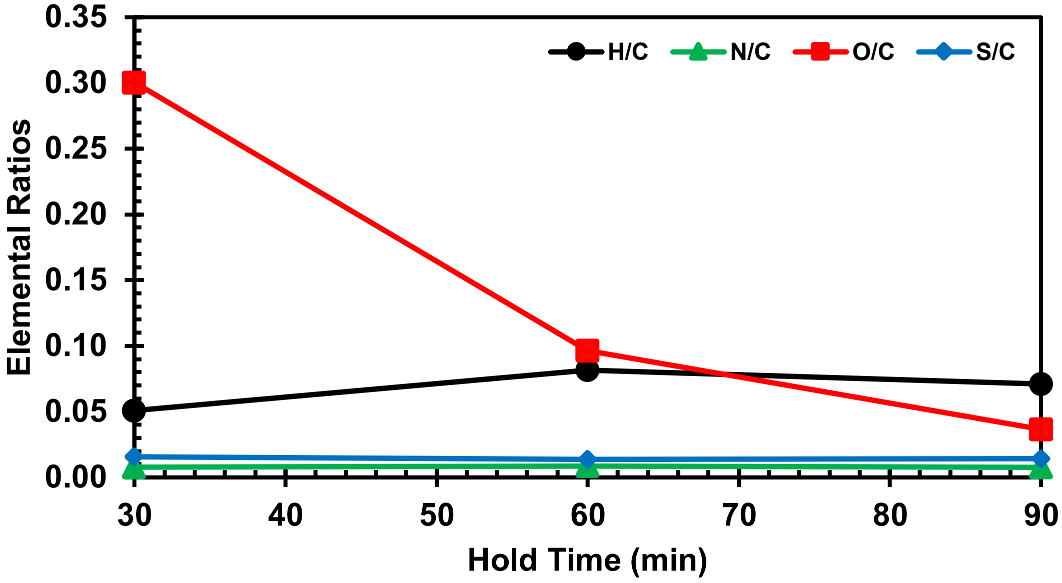

Figure 31: Elemental ratios compared to different oxidation hold times

Figure 31 illustrates that the hold time does not affect the N/C and S/C ratio for the given oxidation and carbonization conditions. When looking at the H/C ratio, the H/C content follows a slight upward trend as the hold time increases but experiences little changes in the H/C ratio. The O/C ratio decreases drastically as the hold time increases.

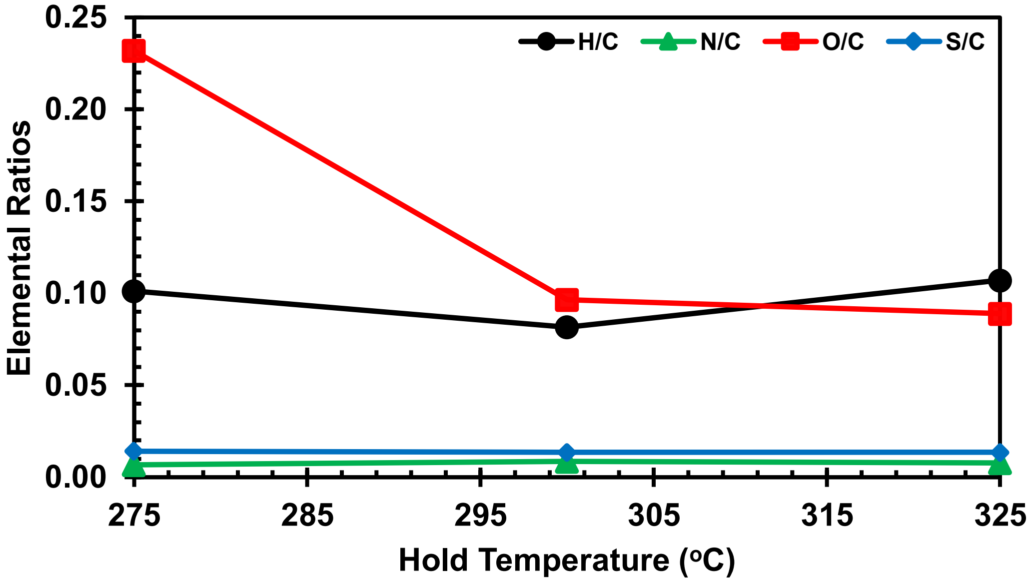

Figure 32: (NOS)/C and H/C ratio compared to different oxidation hold temperature

Figure 32 indicates no relationship between the hold temperature and N/C and S/C ratios, as they do not change as the hold temperature changes. When looking at the H/C ratio, there are not many changes to the H/C content, and the oxidation hold temperature does not significantly affect the resultant H/C content. This could be because the temperature range is relatively small, and an increase/decrease of only 25°C may not be high enough to warrant large variations. The O/C content decreases significantly as the hold temperature increases.

5.4.4 Raman Spectroscopy – Defect Analysis

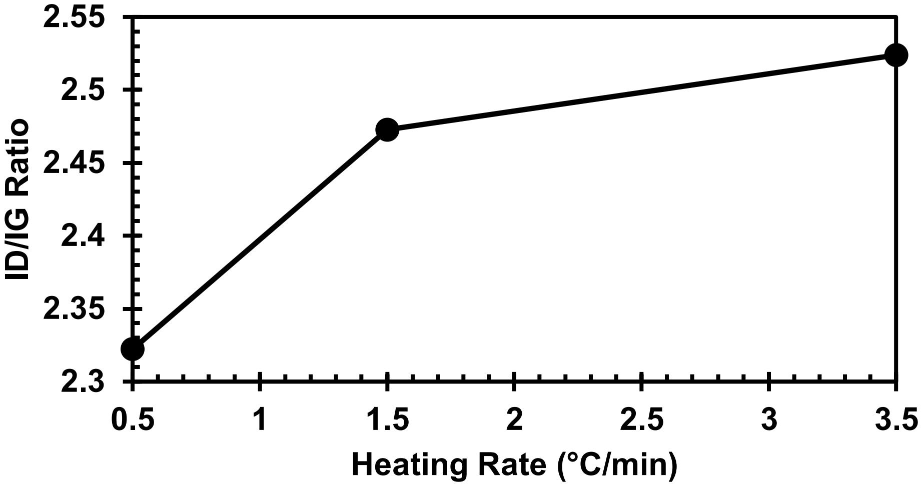

Figure 33: I_D/I_G Ratios at different oxidation heating rates at a carbonization temperature of 800°C

From Figure 33, the defect ratio increases with the heating rate at a rapid rate but then grows slower following the peak value at 1.5°C/min. This indicates that increasing the heating rate could potentially induce more defects in the material.

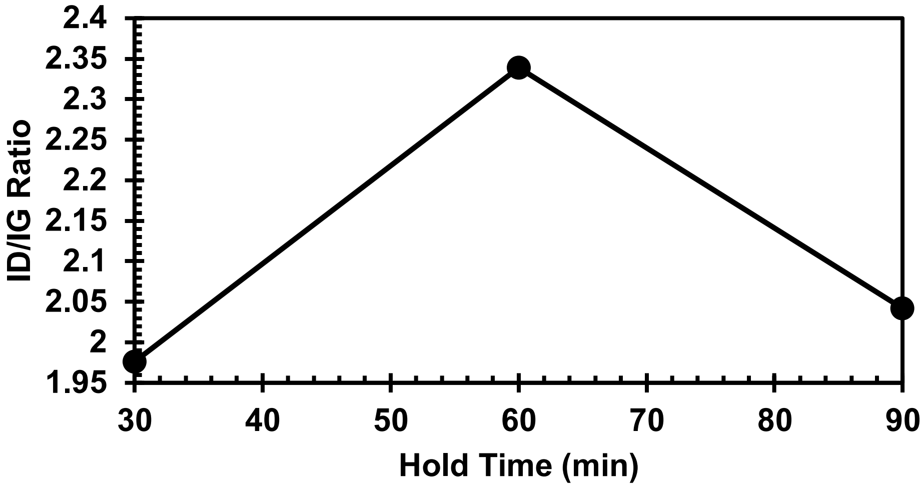

Figure 34: I_D/I_G Ratios at different oxidation holding times at a carbonization temperature of 1200°C

Figure 34 shows that the defect ratio increases with increasing hold time until it reaches a peak of 60 min, followed by a substantial decrease in defect ratio as the hold time increases.

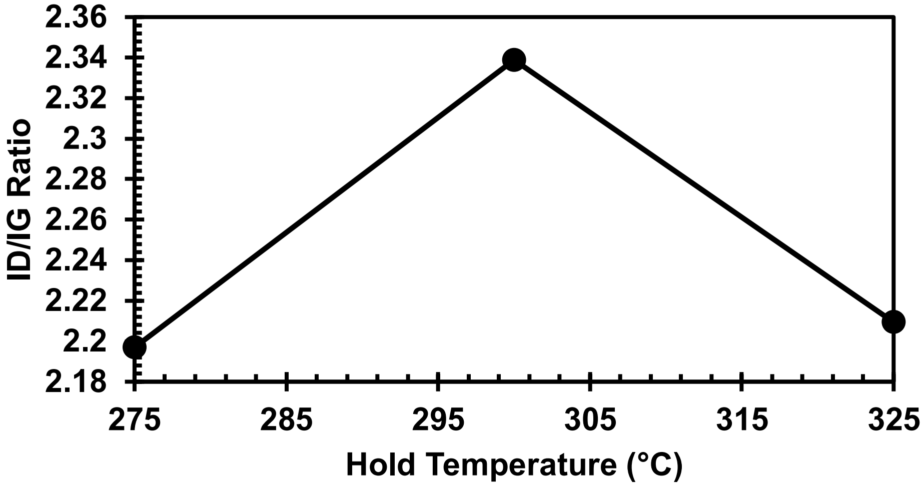

Figure 35: I_D/I_G ratios at different oxidation holding temperatures at a carbonization temperature of 1200°C

Figure 35 demonstrates that the defect ratio increases until the maximum defect ratio is observed at 300°C. A decreasing defect ratio follows this as the hold temperature rises past 300°C.

5.4 Discussion

The analysis across Figures 15, 16, and 17 indicates that mass changes found during oxidation present a parabolic trend for each of the three tests. This could be attributed to the balance between mass gain from the oxidative incorporation of functional groups and mass loss due to the volatilization of inhomogeneous components in the asphaltenes and gaseous phases from reaction with oxygen. Introducing oxygen as carbonyls during oxidation is believed to be accompanied by weight gain [2]. Therefore, the degree of stabilization is highly linked to the extent of oxidation. This is further supported by the physical differences between "insufficient" and "sufficient" oxidized samples, as seen in Figures 36 and 37.

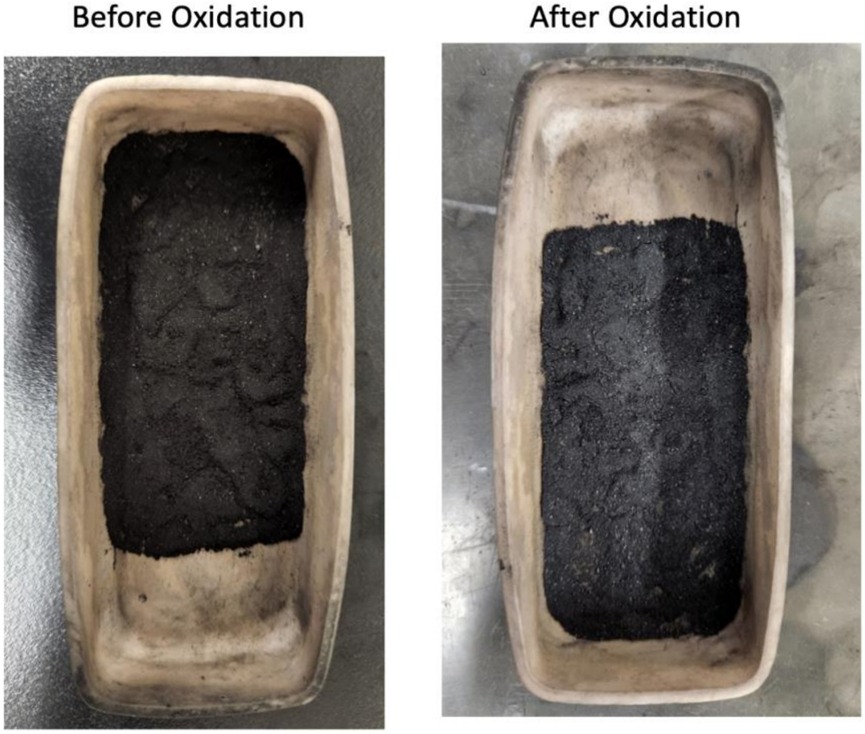

Figure 36: No melting observed under sufficient oxidative stabilization conditions

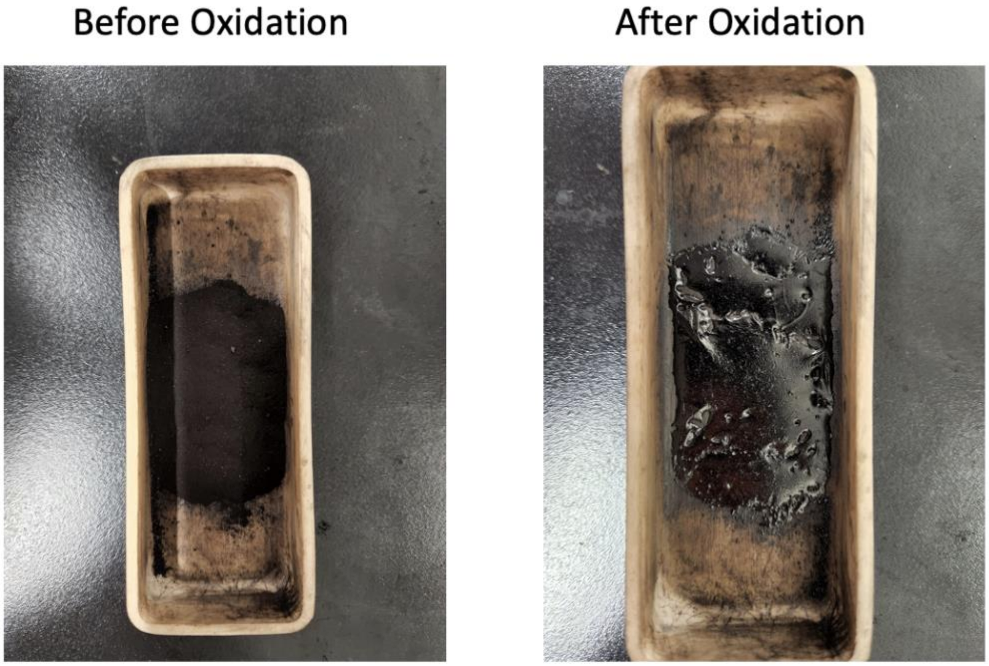
Before Oxidation

After Oxidation

Figure 37: Melting observed after insufficient oxidation stabilization conditions

It is reasonable to assume that the oxidation process will raise the softening point and produce a network unable to melt, which would thermolyze to carbon without ever having to go through a liquid state [2]. Introducing oxygen groups early in the material's treatment stabilizes the structure, reducing reactivity during high-temperature carbonization. This stabilization likely mitigates the formation of ordered carbonaceous structures by suppressing aromatic condensation reactions, as mentioned previously.

The correlation between treatment conditions and d-spacing, as detailed in Figures 21, 23, and 25, highlights the specific conditions of 300°C hold temperature, 60 minutes hold time, 1.5°C/min heating rate, and 800°C carbonization temperature, which maximizes d-spacing. The shifts in maximum peak locations in the d(002) region suggest that temperature, hold time and heating rate all influence the hard carbon’s interlayer spacing.

The trends observed from the (NOS)/C vs. H/C molar ratio plots offer insights into the carbon structure's evolution under treatment:

- A reduction in the H/C ratio post-oxidation and further during carbonization suggests a shift toward a more aromatic structure, indicative of a decrease in aliphatic hydrogen content and an increase in condensed aromatic rings.
- The maintenance of a (NOS)/C ratio after carbonization implies that the introduced heteroatoms are retained, maintaining the structure's complexity and potentially contributing to its electrochemical properties.

The lower H/C ratios, particularly in samples carbonized at 1200°C, indicate a significant move toward an aromatic structure, which could suggest the onset of graphitization. The heating rate is inverse to the H/C ratio, likely due to greater degrees of dehydrogenation at higher temperatures. In contrast, the O/C ratio increases slightly with the heating rate, possibly indicating a more efficient incorporation of oxygen at higher temperatures.

As for the hold time, an initial increase in the H/C ratio could be due to the thermal stabilization of volatile components. However, this peaks at a hold time of 60 minutes, beyond which the ratio decreases, indicating a progressive loss of hydrogen content with extended hold times. The decline in the O/C ratio with increasing hold time might be due to the enrichment of the carbon framework, reducing the relative number of oxygen and other heteroatoms. It makes sense that the H/C ratio is almost inverse to the O/C ratio, as the weight gain of oxygen is accompanied by the loss of methylene hydrogens [2].

Increasing hold temperatures do not significantly affect the H/C ratio, suggesting a threshold beyond which further thermal treatment does not induce substantial dehydrogenation. The negative trend in the O/C ratio with higher hold temperatures could be explained by the conversion of C to CO_2, which may occur faster at higher hold temperatures.

A high I_D/I_G ratio points to a large degree of disorder. This disorder is characterized by increased defects, which may benefit sodium-ion diffusion, leading to more active sites and miffusion pathways. Increased defects, as evidenced by higher I_D/I_G ratios with rising heating rates, provide additional sites for sodium-ion storage, potentially enhancing the hard carbon's capacity.

Optimal defect creation appears to be achieved at a hold time and temperature of 60 minutes and 300°C. This could be used in the future to fine-tune the electrochemical properties.

5.5 Conclusion

This study has shed light on the relationship between treatment oxidation parameters and the properties of asphaltene-derived hard carbons. The results highlight the critical nature of oxidative stabilization in influencing the material's mass, structure, and elemental composition. A balance between mass gain from oxidative processes and mass loss due to volatile release was discovered, emphasizing the need for process optimization. The optimal treatment conditions were 300°C for 60 minutes at a heating rate of 1.5°C/min and carbonization at 800°C. These conditions significantly enhanced the carbon's interlayer spacing and electrochemical capabilities. The changes in the H/C and (NOS)/C molar ratios observed post-carbonization suggest a successful shift toward a more aromatic structure with retained heteroatoms, beneficial to electrochemical performance. The increased I_D/I_G ratio points to disorder within the carbon matrix, potentially being able to improve sodium-ion diffusion and storage.

5.6 References

[1] P.-Y. Zhao, J.-J. Tang, and C. Wang, “A low-cost attempt to improve electrochemical performances of pitch-based hard carbon anodes in lithium-ion batteries by oxidative stabilization,” *Journal of Solid State Electrochemistry*, vol. 21, no. 2, pp. 555–562, Sep. 2016, doi: https://doi.org/10.1007/s10008-016-3406-1.

[2] J. Drbohlav and William, “The oxidative stabilization and carbonization of a synthetic mesophase pitch, part I: The oxidative stabilization process,” vol. 33, no. 5, pp. 693–711, Jan. 1995, doi: https://doi.org/10.1016/0008-6223(95)00011-2.

Chapter 6 – Modification of Carbonization Parameters

6.1 Introduction

This section examines the influence of carbonization parameters on the interlayer d-spacing of carbonaceous samples. The focus is on the effect of heating rate and holding temperature during carbonization. The core objectives were to understand how these variations would affect the properties of the resultant hard carbon and to optimize these conditions to enhance the d-spacing and defects.

The carbonization process is crucial for the transformation of asphaltenes into hard carbons, encompassing the following fundamental reactions and changes:

- Thermal decomposition in an oxygen-restricted environment to prevent combustion and facilitate the breakdown of organic materials into carbon structures.
- Progressive annealing in an inert atmosphere allows for the systematic release of volatile matter, which enriches the carbon content as non-carbon elements like hydrogen and oxygen are removed.
- Subsequent structural rearrangements lead to enhanced aromaticity via dehydration reactions.
- Improved structural integrity through cross-linking and polycondensation.
- Reduction in heteroatoms and other functional groups introduced during prior oxidative stabilization.

In examining the impact of carbonization parameters on the final properties of the resultant hard carbons, we observed critical trends related to heating rates, temperature, and resulting structural changes. The decision to adjust carbonization parameters stemmed from the premise that these variables, hold time, hold temperature, and heating rate, dictate the rate of reactions and the evolution of volatile by-products, which in turn influence the final material's characteristics. Our findings are instrumental in understanding how to optimize conditions for producing carbon materials suitable for sodium-ion batteries.

Batch B56, as listed in Table A1, Appendix A**,** was selected for its large d-spacing observed during oxidative stabilization trials and served as the standard feedstock for the proceeding carbonization experiments. This batch utilized a particle size of 53.7 µm and the oxidation conditions of B56, comprising a hold temperature of 300°C, a hold time of 60 minutes, and a heating rate of 1.5°C/min. A large batch was processed to ensure consistency, setting a controlled baseline for assessing the outcomes of the modified carbonization parameters.

6.2 Experimental Procedure

The experiment followed the procedure outlined in Chapter 3 for the oxidative stabilization and carbonization process. The experimental methodology was slightly altered with these separate conditions:

1. **Carbonization Temperature:** This set of experiments examined a temperature bracket ranging from 800°C to 1500°C.

2. **Heating Rate:** The heating rate was adjusted from 0.5°C/min to 10°C/min.

By examining these parameters, this chapter analyzes the carbonization process to improve the treatment process further.

Table 4: Carbonization treatment conditions

Carbonization Temperature (°C)	Heating Rate (°C/min)
800	0.5
1000	1
1200	3
1500	5
	10

6.3 Results

6.3.1 Mass Changes

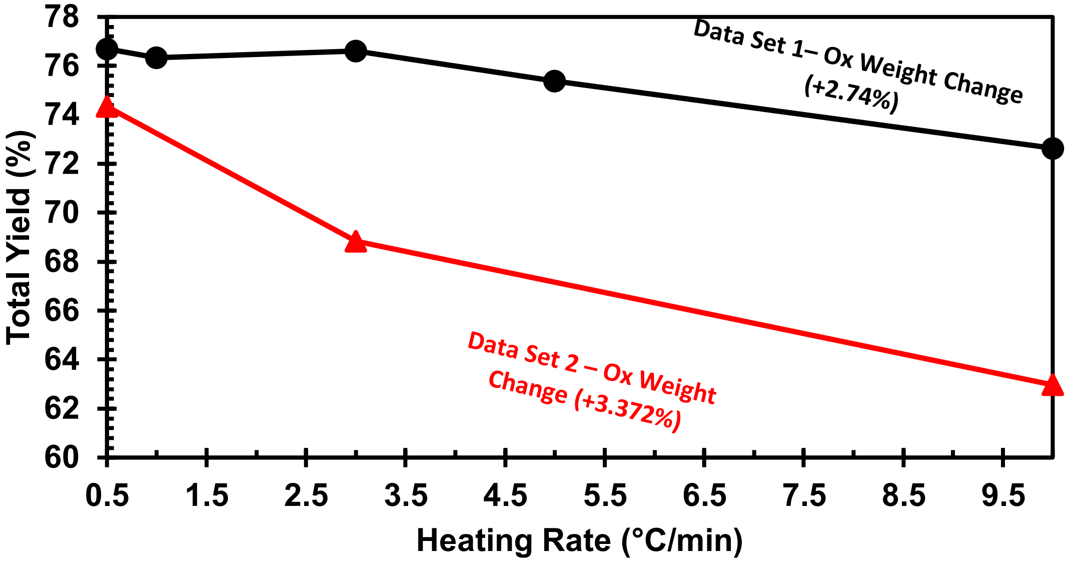

Figure 38: Total yield for different carbonization heating rates at 800°C for 120 min

Figure 38 demonstrates the differences in total yield post-carbonization. It was repeated with another set of oxidized materials under the same conditions, as each batch achieved different oxidation weight changes even with identical conditions. This is denoted by data sets 1 and 2. Both data sets show that the yield decreases as the heating rate increases. This indicates that the carbonization heating rate influences the final product's yield.

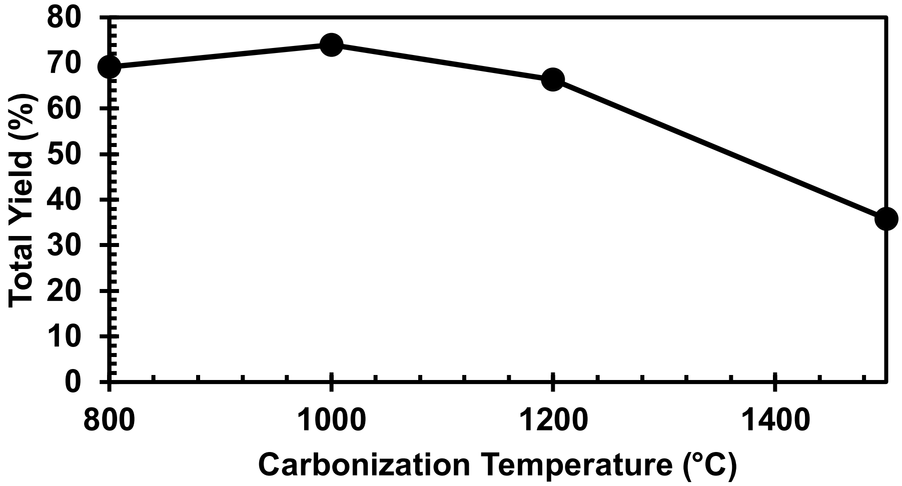

Figure 39: Total yield for different carbonization temperatures at a heating rate of 3°C for 120 min

In Figure 39, the yield increases slightly from 800°C to a maximum observed at 1000°C. This is then followed by a decline in yield as the carbonization temperature increases. This indicates that the carbonization temperature has a significant impact on the total yield of the product.

6.3.2 Interplanar Spacing with XRD

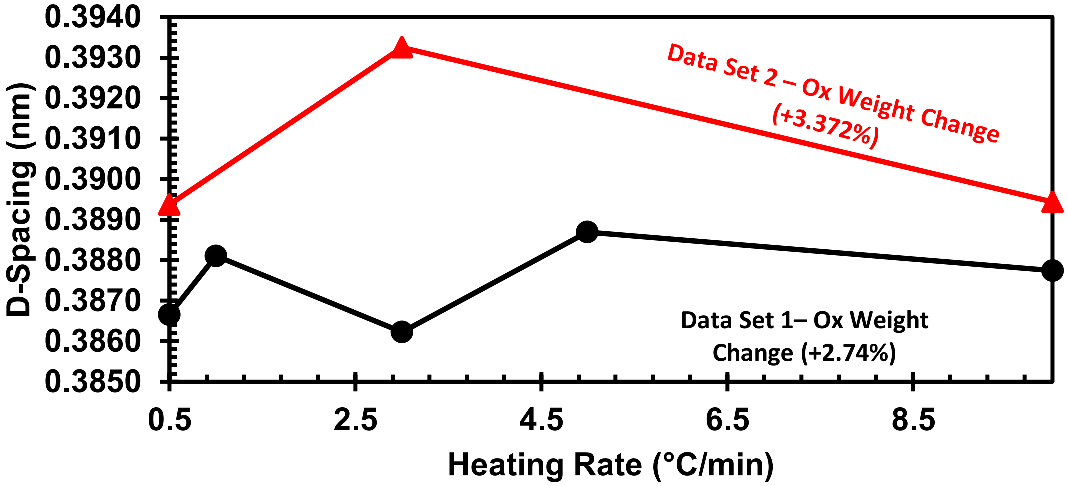

Figure 40: D-Spacing for different carbonization heating rates at 800°C for 120 min

Figure 40 shows that the d-spacing increases initially with an increasing heating rate for data set 2 but then reduces d-spacing following heating rates above 3°C/min after it reaches the maximum peak. On the other hand, data set 1 showed some fluctuations in d-spacing, making it difficult to observe a trend. The results demonstrated in Data Set 1 may not be representative of the material behaviour, as the point at 3°C/min is significantly lower compared to the point in Data Set 2, and that skews the whole curve.

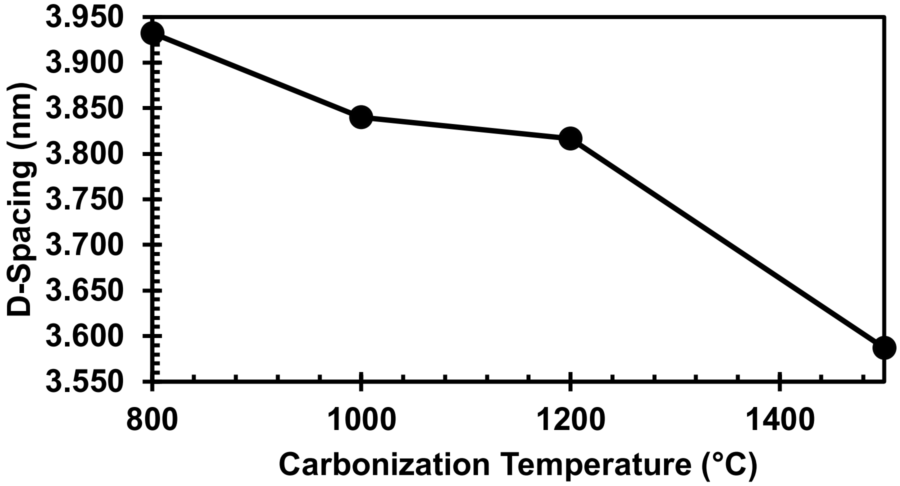

Figure 41: D-Spacing for different carbonization temperatures at a heating rate of 3°C/min for 120 min

Figure 41 shows a negative relationship between the d-spacing and carbonization temperature. The d-spacing steadily decreases with increasing carbonization temperature. This indicates the transition from more amorphous characteristics to a more crystalline nature of graphite.

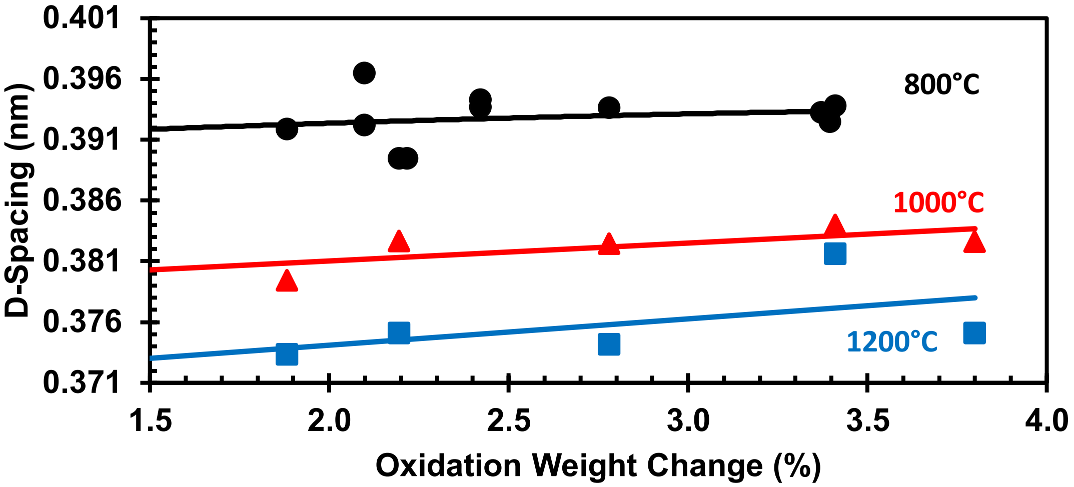

Figure 42: D-Spacing for different oxidation weight changes for differing carbonization temperatures

Figure 42 plots all data for the oxidation weight changes for oxidation heating rate experiments utilizing different carbonization temperatures. This was plotted together to understand better the relationship between the oxidation weight changes and the resultant d-spacing. Figure 42 shows that they all have a range of d-spacing that the samples can revolve around. The highest d-spacing is observed for carbonization temperatures of 800°C, which decreases as the temperature increases.

6.3.3 Elemental Composition

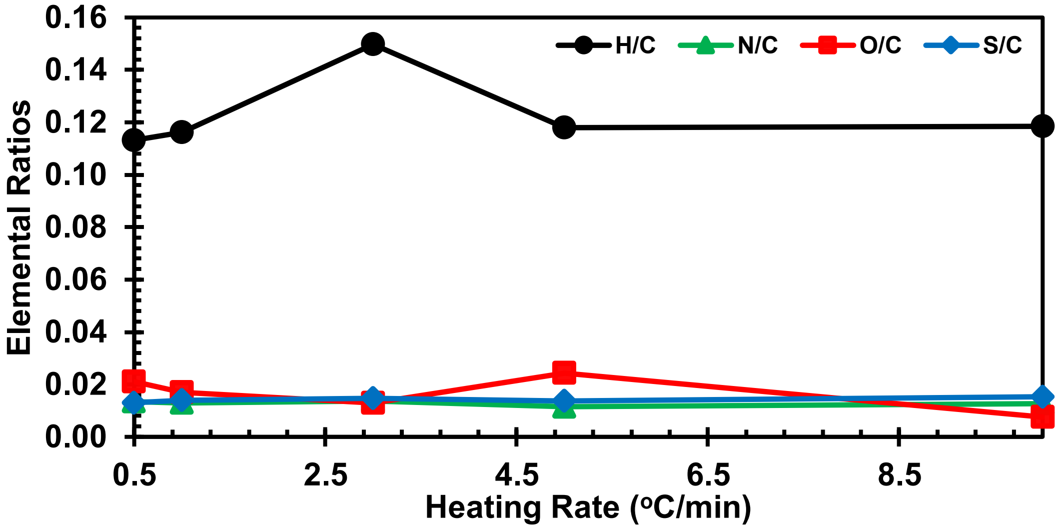

Figure 43: Elemental ratios for different carbonization heating rates

Figure 43 indicates that the heating rate has little effect on the elemental composition. For nitrogen and sulfur, there is almost no effect on the elemental ratios. The oxygen content is also slightly affected and decreases somewhat with increasing heating rate. When looking at the H/C ratio, most of the H/C ratios show little change and hover around a ratio of 0.12 but spike at a heating rate of 3°C/min. This could be due to experimental error or inherent material properties.

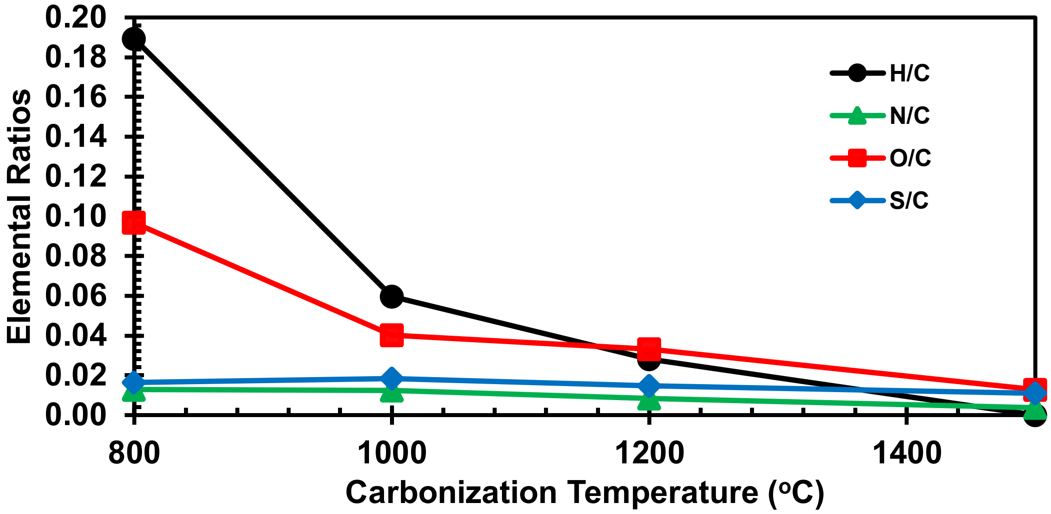

Figure 44: Elemental ratios for different carbonization temperatures

Figure 44 shows a strong negative trend between the H/C ratio and the carbonization temperature. The H/C ratio begins relatively high and drops significantly as the carbonization temperature increases. It is also interesting to note that while there has been almost no effect on the N/C and S/C ratio for other experiments, it can be seen that they both decrease slightly with increasing carbonization temperature. The O/C ratio also decreases as the carbonization temperature rises over time.

6.3.4 Raman Spectroscopy

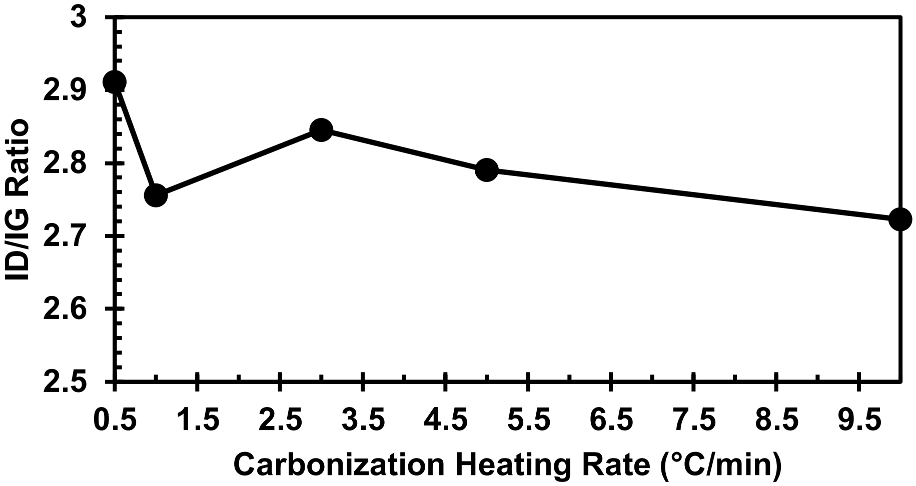

Figure 45: I_D/I_G ratios at different carbonization heating rates at 800°C for 120 min

Figure 45 indicates a negative relationship between the I_D/I_G ratios and the carbonization heating rate. As the carbonization heating rate increases, the defect ratio decreases accordingly.

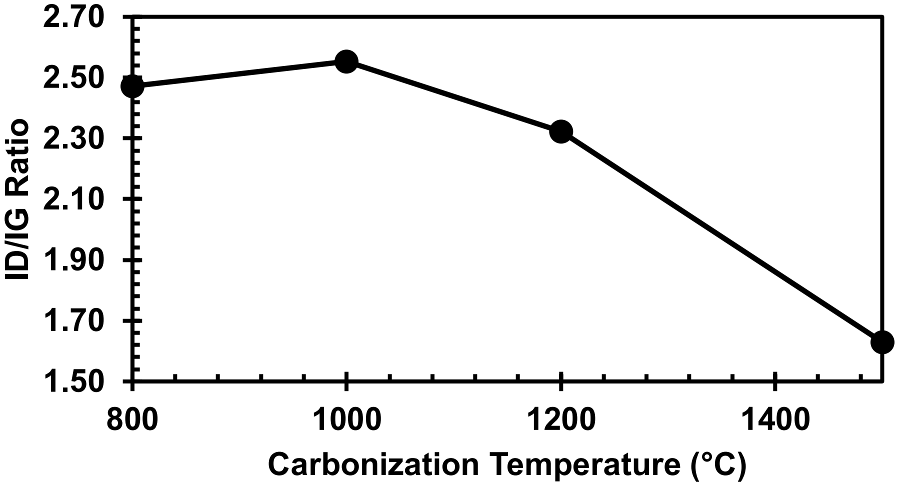

Figure 46: I_D/I_G ratios at different carbonization temperatures at 3°C/min for 120 min

In Figure 46, the defect ratio rises slightly to reach a maximum of 1000°C and decreases substantially as the carbonization temperature increases.

6.4 Discussion

The trends observed may indicate a correlation between the rate and the volatility of the reaction. At a lower heating rate, such as 0.5°C/min, the process was more gradual, which allowed for a more complete evolution of gases. This resulted in a higher yield even with a lengthy treatment time of 1480 minutes. In contrast, a higher rate, like 5°C/min with a reduced treatment time of 148 minutes, seemed to have a less controlled evolution of volatiles, which resulted in a lower yield. When compared to other studies that utilize pitch as the main precursor, it is seen that from the 30-850ºC range, the released mixture of aromatic compounds and volatile small molecules contain compounds such as CO, CO_2, CH_4, and leave behind hydrocarbon skeletons after being expelled [2]. Compared to the oxidation experiments, it can be seen that oxidative stabilization aims to integrate oxygen into the material, while carbonization focuses on expelling it. It is found that medium to low heating rates in both stages maximized oxygen content, thus increasing d-spacing.

The carbonization temperature displayed a significant impact on the material's structural properties. Reduced yield at higher temperatures led to temperature-dependent reactions that facilitated the loss of non-carbon elements. This was illustrated by the decrease in both H/C and (NOS)/C ratios at elevated temperatures, indicating a more efficient purging of heteroatoms, directly contributing to increased carbon content.

Moreover, the correlation between increased carbonization temperature and decreased d-spacing was consistent with the theory of graphitization. At higher temperatures above 1200°C, the enhanced alignment of layers led to a reduction in d-spacing. This could limit ion mobility, which is detrimental to sodium-ion battery applications. It is suggested that an intrinsic trend of carbon materials is decreasing interplanar spacing with increasing carbonization temperature, which is unfavourable for the capacity, but the more ordered structure is beneficial to the coulombic efficiency at higher temperatures [5].

Raman analysis highlighted that samples treated at 1000°C had the highest defect ratio. Defects in carbon materials can be beneficial, serving as active sites for sodium-ion intercalation.

Therefore, carbonizing future samples at this temperature might strike a balance between creating beneficial defects and achieving an adequate d-spacing for ion transport.

6.5 Conclusion

In conclusion, it was deemed that carbonization parameters have a critical role in carbon materials' structural and electrochemical characteristics. The findings indicate that lower heating rates favour a higher carbon yield and potentially enhance battery performance by allowing for a greater d-spacing. Carbonization temperature also influences the degree of graphitization and interplanar spacing. The optimal carbonization temperature appears to be around 1000°C, considering both yield and defect ratio, but a temperature of 800°C was observed for the highest amount of d-spacing. The balance between the oxidative stabilization and carbonization processes reveals that high oxygen content is crucial for achieving the desired d-spacing, thereby improving the material's suitability for energy storage applications.

6.6 References

[1] H. Hu and M. Wu, “Heavy oil-derived carbon for energy storage applications,” *Journal of materials chemistry. A, Materials for energy and sustainability*, vol. 8, no. 15, pp. 7066–7082, Jan. 2020, doi: https://doi.org/10.1039/d0ta00095g.

[2] Q. Lin, T. Li, C. Zheng, Y. Zhao, and S. Song, “Carbonization behaviour of coal-tar pitch modified with divinylbenzene and optical texture of resultant semi-cokes,” *Journal of Analytical and Applied Pyrolysis*, vol. 71, no. 2, pp. 817–826, Jun. 2004, doi: https://doi.org/10.1016/j.jaap.2003.10.009.

[3] L. Xiao *et al.*, “Low-Defect and Low-Porosity Hard Carbon with High Coulombic Efficiency and High Capacity for Practical Sodium Ion Battery Anode,” *Advanced Energy Materials*, vol. 8, no. 20, p. 1703238, Mar. 2018, doi: https://doi.org/10.1002/aenm.201703238.

[4] S. Qiu *et al.*, “Manipulating Adsorption–Insertion Mechanisms in Nanostructured Carbon Materials for High-Efficiency Sodium Ion Storage,” *Advanced Energy Materials*, vol. 7, no. 17, p. 1700403, May 2017, doi: https://doi.org/10.1002/aenm.201700403.

[5] P.-Y. Zhao, Y. Guo, B.-J. Yu, J. Zhang, and C.-Y. Wang, “Biotechnology humic acids-based electrospun carbon nanofibers as cost-efficient electrodes for lithium-ion batteries,” *Electrochimica Acta*, vol. 203, pp. 66–73, Jun. 2016, doi: https://doi.org/10.1016/j.electacta.2016.03.109.

Chapter 7 – Conclusions and Recommendations

7.1 Limitations

Several limitations have been encountered during this study, which is essential to acknowledge as they offer context for the results and may help guide future work.

Uniformity in Sample Preparation: The fine grinding of the raw material was essential for the experiments, yet it introduced a challenge. The tendency of the finely ground particles to clump together made uniform dispersion across the crucible challenging. This uneven distribution could affect the consistency of the heat treatment processes, leading to variability within the sample.

Oxygen Penetration During Oxidation: The compact particles could make it difficult for the oxygen to permeate uniformly, potentially resulting in gradients of oxidation within a single sample. This could mean the sample mass's exterior might be over-oxidized while the interior might not oxidize sufficiently. This variability made it difficult to produce large, homogenous batches for experimental trials, which led to the production of multiple 1g batches combined to standardize the sample set.

R**epeatability and Reliability of Samples:** The sensitivity of the samples to their treatment conditions meant that some required repeating due to significant deviation from expected results. Deciding which samples to consider reliable was complex, as minor variations had profound impacts on the subsequent characterization of the material.

X-ray Diffraction (XRD) Complications: Challenges arose in using X-ray diffraction (XRD) for material characterization. The methodological choice to employ a Gaussian line fitting function for XRD data processing may have been better for analyzing full XRD spectrum patterns versus a small area within the (002) region. Initial characterizations were conducted over a small angle range to conserve time. However, transitions between different XRD stages (standard stage to ASC-10 Stage to thin film stage) led to slight, yet impactful, deviations in XRD patterns. There were also challenges in the accuracy of the XRD results due to general machine error and sample preparation. It is difficult to guarantee the same measurements for each sample, as small changes can significantly affect the results. An internal measurement was done to help affirm the results and show that there is only a slight deviation in results. However, this must be conducted for each run in future experiments to allow for greater minimization of errors.

Human and Equipment Error: The potential for human error cannot be eliminated. Moreover, any experimental setup is susceptible to equipment errors, which may influence the precision and accuracy of the results.

Recognizing these limitations is essential for interpreting the current work and future research directions. Efforts to mitigate these issues could involve exploring alternative methods for ensuring sample uniformity, refining XRD techniques, and experimenting with new strategies for characterizing and processing fine asphaltene particles. By addressing these challenges, we can further advance asphaltene-derived hard carbons.

7.2 Conclusion and Recommendations

In this thesis, the relationship between a broad range of treatment parameters and the properties of the asphaltene-derived hard carbons was explored with a focus on the optimization of sodium-ion battery anodes. It is established that the optimal parameters influence the d-spacing within asphaltene-derived hard carbons through a series of controlled experiments. The oxidative stabilization process at 300°C for 60 minutes with a heating rate of 1.5°C/min, followed by a carbonization process at 800°C for 120 minutes at a heating rate of 3°C/min, emerged as the most influential parameters for achieving the highest d spacing.

The correlation between oxidative weight gain and d-spacing has been observed, indicating that as the weight gained during oxidation increases, so does d-spacing, which is advantageous for sodium-ion storage. A key finding is precisely controlling oxygen content within the carbon matrix. The proper oxygen balance is critical, as under- and over-oxidation can severely impact the material's performance in a potential battery. The defect structure, as shown by I_D/I_G ratio, also plays a significant role. An increase in defects correlates with an increase in d-spacing, which offers more sites for sodium-ion intercalation and thereby enhances the electrochemical performance.

While general trends could be found in this thesis for the effects of oxidation and carbonization on the properties of a resulting asphaltene-derived hard carbon, it also opens the door to future studies. In particular, investigations into the creation of ultra-micropores could lead to significant advances, as these structures are expected to enhance sodium-ion intercalation chemistry, further improving ion diffusion and charge transfer kinetics in battery materials. Chemical activation could be a method for tailoring this porosity, and incorporating a range of pore sizes could further optimize the material for sodium-ion battery use.

Optimizing treatment parameters at each stage has demonstrated the potential for advancements in developing hard carbons for sodium-ion battery anodes. The insights gained contribute serve as stepping stones for future research to refine and implement these findings into practical applications.

Bibliography

C. Bommier and X. Ji, “Electrolytes, SEI Formation, and Binders: A Review of Nonelectrode Factors for Sodium-Ion Battery Anodes,” *Small*, vol. 14, no. 16, p. 1703576, Jan. 2018, doi: https://doi.org/10.1002/smll.201703576.

D. Alvira, D. Antorán, and J. J. Manyà, “Plant-derived hard carbon as anode for sodium-ion batteries: A comprehensive review to guide interdisciplinary research,” *Chemical Engineering Journal*, vol. 447, p. 137468, Nov. 2022, doi: https://doi.org/10.1016/j.cej.2022.137468.

D. Saurel, B. Orayech, B. Xiao, D. Carriazo, X. Li, and T. Rojo, “From Charge Storage Mechanism to Performance: A Roadmap toward High Specific Energy Sodium-Ion Batteries through Carbon Anode Optimization,” *Advanced Energy Materials*, vol. 8, no. 17, p. 1703268, Mar. 2018, doi: https://doi.org/10.1002/aenm.201703268.

F. Soto *et al.*, “Tuning the Solid Electrolyte Interphase for Selective Li- and Na-Ion Storage in Hard Carbon,” vol. 29, no. 18, pp. 1606860–1606860, Mar. 2017, doi: https://doi.org/10.1002/adma.201606860.

G. Zou, H. Hou, G. Zhao, Z. Huang, P. Ge, and X. Ji, “Preparation of S/N-codoped carbon nanosheets with tunable interlayer distance for high-rate sodium-ion batteries,” *Green Chemistry*, vol. 19, no. 19, pp. 4622–4632, 2017, doi: https://doi.org/10.1039/c7gc01942d.

H. Hu and M. Wu, “Heavy oil-derived carbon for energy storage applications,” *Journal of materials chemistry. A, Materials for energy and sustainability*, vol. 8, no. 15, pp. 7066–7082, Jan. 2020, doi: https://doi.org/10.1039/d0ta00095g.

H. Hu and M. Wu, “Heavy oil-derived carbon for energy storage applications,” *Journal of materials chemistry. A, Materials for energy and sustainability*, vol. 8, no. 15, pp. 7066–7082, Jan. 2020, doi: https://doi.org/10.1039/d0ta00095g.

H. Marsh, In Introduction to Carbon Science (Edited by H. Marsh), Chapter 3. Butterworths, London (1989).

İ. Gergin, E. Ismar, and A. S. Sarac, “Oxidative stabilization of polyacrylonitrile nanofibers and carbon nanofibers containing graphene oxide (GO): a spectroscopic and electrochemical study,” *Beilstein Journal of Nanotechnology*, vol. 8, pp. 1616–1628, Aug. 2017, doi: https://doi.org/10.3762/bjnano.8.161.

J. Drbohlav and W. T. K. Stevenson, “The oxidative stabilization and carbonization of a synthetic mesophase pitch, part II: The carbonization process,” *Carbon*, vol. 33, no. 5, pp. 713–731, 1995, doi: https://doi.org/10.1016/0008-6223(95)00012-3.

J. Drbohlav and William, “The oxidative stabilization and carbonization of a synthetic mesophase pitch, part I: The oxidative stabilization process,” vol. 33, no. 5, pp. 693–711, Jan. 1995, doi: https://doi.org/10.1016/0008-6223(95)00011-2.

J. G. Speight, “A Review of: ‘The Chemistry of Alberta Oil Sands Bitumens and Heavy Oils,’” *Energy Sources*, vol. 27, no. 8, pp. 780–780, Jun. 2005, doi: https://doi.org/10.1080/00908310590967283.

K. Yu, X. Wang, H. Yang, Y. Bai, and C. Wu, “Insight to defects regulation on sugarcane waste-derived hard carbon anode for sodium-ion batteries,” *Journal of Energy Chemistry*, vol. 55, pp. 499–508, Apr. 2021, doi: https://doi.org/10.1016/j.jechem.2020.07.025.

L. Liu, Y. Tian, A. Abdussalam, M. R. H. S. Gilani, W. Zhang, and G. Xu, “Hard Carbons as Anodes in Sodium-Ion Batteries: Sodium Storage Mechanism and Optimization Strategies,” *Molecules*, vol. 27, no. 19, p. 6516, Oct. 2022, doi: https://doi.org/10.3390/molecules27196516.

L. Xiao *et al.*, “Low-Defect and Low-Porosity Hard Carbon with High Coulombic Efficiency and High Capacity for Practical Sodium Ion Battery Anode,” *Advanced Energy Materials*, vol. 8, no. 20, p. 1703238, Mar. 2018, doi: https://doi.org/10.1002/aenm.201703238.

L. Xiao *et al.*, “Low-Defect and Low-Porosity Hard Carbon with High Coulombic Efficiency and High Capacity for Practical Sodium Ion Battery Anode,” *Advanced Energy Materials*, vol. 8, no. 20, p. 1703238, Mar. 2018, doi: https://doi.org/10.1002/aenm.201703238.

M. Cabello *et al.*, "On the Reliability of Sodium Co-Intercalation in Expanded Graphite Prepared by Different Methods as Anodes for Sodium-Ion Batteries," *Journal of The Electrochemical Society*, vol. 164, no. 14, pp. A3804–A3813, Jan. 2017, doi: https://doi.org/10.1149/2.0211714jes.

M. Hassanzadeh and M. Abdouss, "Essential role of structure, architecture, and intermolecular interactions of asphaltene molecules on properties (self-association and surface activity)," *Heliyon*, vol. 8, no. 12, p. e12170, Dec. 2022, doi: https://doi.org/10.1016/j.heliyon.2022.e12170.

M. I. Jamesh and A. S. Prakash, "Advancement of technology towards developing Na-ion batteries," *Journal of Power Sources*, vol. 378, pp. 268–300, Feb. 2018, doi: https://doi.org/10.1016/j.jpowsour.2017.12.053.

M. Kamkar and G. Natale, "A review on novel applications of asphaltenes: A valuable waste," *Fuel*, vol. 285, p. 119272, Feb. 2021, doi: https://doi.org/10.1016/j.fuel.2020.119272.
M. L. Chacón-Patiño *et al.*, "Lessons Learned from a Decade-Long Assessment of Asphaltenes by Ultrahigh-Resolution Mass Spectrometry and Implications for Complex Mixture Analysis," vol. 35, no. 20, pp. 16335–16376, Oct. 2021, doi: https://doi.org/10.1021/acs.energyfuels.1c02107.

P. Liu, Y. Li, Y.-S. Hu, H. Li, L. Chen, and X. Huang, "A waste biomass derived hard carbon as a high-performance anode material for sodium-ion batteries," *Journal of Materials Chemistry A*, vol. 4, no. 34, pp. 13046–13052, 2016, doi: https://doi.org/10.1039/c6ta04877c.

P.-Y. Zhao, J.-J. Tang, and C. Wang, "A low-cost attempt to improve electrochemical performances of pitch-based hard carbon anodes in lithium-ion batteries by oxidative stabilization," *Journal of Solid State Electrochemistry*, vol. 21, no. 2, pp. 555–562, Sep. 2016, doi: https://doi.org/10.1007/s10008-016-3406-1.

P.-Y. Zhao, J.-J. Tang, and C. Wang, "A low-cost attempt to improve electrochemical performances of pitch-based hard carbon anodes in lithium-ion batteries by oxidative stabilization,” *Journal of Solid State Electrochemistry*, vol. 21, no. 2, pp. 555–562, Sep. 2016, doi: https://doi.org/10.1007/s10008-016-3406-1.

P.-Y. Zhao, J.-J. Tang, and C. Wang, “A low-cost attempt to improve electrochemical performances of pitch-based hard carbon anodes in lithium-ion batteries by oxidative stabilization,” *Journal of Solid State Electrochemistry*, vol. 21, no. 2, pp. 555–562, Sep. 2016, doi: https://doi.org/10.1007/s10008-016-3406-1.

Q. Lin, T. Li, C. Zheng, Y. Zhao, and S. Song, “Carbonization behaviour of coal-tar pitch modified with divinylbenzene and optical texture of resultant semi-cokes,” *Journal of Analytical and Applied Pyrolysis*, vol. 71, no. 2, pp. 817–826, Jun. 2004, doi: https://doi.org/10.1016/j.jaap.2003.10.009.

R. Zhao, N. Sun, and B. Xu, “Recent Advances in Heterostructured Carbon Materials as Anodes for Sodium-Ion Batteries,” *Small structures*, vol. 2, no. 12, Oct. 2021, doi: https://doi.org/10.1002/sstr.202100132.

R. Zhao, N. Sun, and B. Xu, “Recent Advances in Heterostructured Carbon Materials as Anodes for Sodium-Ion Batteries,” *Small structures*, vol. 2, no. 12, Oct. 2021, doi: https://doi.org/10.1002/sstr.202100132.

S. Mukherjee, S. Bin Mujib, D. Soares, and G. Singh, “Electrode Materials for High-Performance Sodium-Ion Batteries,” *Materials*, vol. 12, no. 12, p. 1952, Jun. 2019, doi: https://doi.org/10.3390/ma12121952.

S. Qiu *et al.*, “Manipulating Adsorption–Insertion Mechanisms in Nanostructured Carbon Materials for High-Efficiency Sodium Ion Storage,” *Advanced Energy Materials*, vol. 7, no. 17, p. 1700403, May 2017, doi: https://doi.org/10.1002/aenm.201700403.

T. Perveen, M. Siddiq, N. Shahzad, R. Ihsan, A. Ahmad, and M. I. Shahzad, “Prospects in anode materials for sodium ion batteries - A review,” *Renewable and Sustainable Energy Reviews*, vol. 119, p. 109549, Mar. 2020, doi: https://doi.org/10.1016/j.rser.2019.109549.

T. Zhou, S. Yang, Y. Wei, J. Hu, and H. Wang, “Impact of wide particle size distribution on the gasification performance of biomass in a bubbling fluidized bed gasifier,” vol. 148, pp. 534–547, Apr. 2020, doi: https://doi.org/10.1016/j.renene.2019.10.059.

W. Chen, M. Wan, Q. Liu, X. Xiong, F. Yu, and Y. Huang, “Heteroatom-Doped Carbon Materials: Synthesis, Mechanism, and Application for Sodium-Ion Batteries,” *Small Methods*, vol. 3, no. 4, p. 1800323, Oct. 2018, doi: https://doi.org/10.1002/smtd.201800323.

W. Li, S.-L. Chou, J.-Z. Wang, J. H. Kim, H.-K. Liu, and S.-X. Dou, “$Sn_{4+x}P_3$@ Amorphous Sn-P Composites as Anodes for Sodium-Ion Batteries with Low Cost, High Capacity, Long Life, and Superior Rate Capability,” *Advanced Materials*, vol. 26, no. 24, pp. 4037–4042, Apr. 2014, doi: https://doi.org/10.1002/adma.201400794.

W. Luo *et al.*, “Electrochemically Expandable Soft Carbon as Anodes for Na-Ion Batteries,” *ACS Central Science*, vol. 1, no. 9, pp. 516–522, Nov. 2015, doi: https://doi.org/10.1021/acscentsci.5b00329.

W. Zhang, F. Zhang, F. Ming, and H. N. Alshareef, “Sodium-ion battery anodes: Status and future trends,” *EnergyChem*, vol. 1, no. 2, p. 100012, Sep. 2019, doi: https://doi.org/10.1016/j.enchem.2019.100012.

Y. Niu, H. Tan, Y. Liu, X. Wang, and T. Xu, “The Effect of Particle Size and Heating Rate on Pyrolysis of Waste Capsicum Stalks Biomass,” *Energy Sources, Part A: Recovery, Utilization, and Environmental Effects*, vol. 35, no. 17, pp. 1663–1669, Sep. 2013, doi: https://doi.org/10.1080/15567036.2010.509084.

Y. Tang, X. Wang, J. Chen, X. Wang, D. Wang, and Z. Mao, “PVP-assisted synthesis of g–C3N4–derived N-doped graphene with tunable interplanar spacing as high-performance lithium/sodium ions battery anodes,” *Carbon*, vol. 174, pp. 98–109, Apr. 2021, doi: https://doi.org/10.1016/j.carbon.2020.12.010.

Z. Li *et al.*, “Mechanism of Na-Ion Storage in Hard Carbon Anodes Revealed by Heteroatom Doping,” vol. 7, no. 18, pp. 1602894–1602894, May 2017, doi: https://doi.org/10.1002/aenm.201602894.

Appendices

Appendix A: Extra Data

Table A1: Table of oxidation and carbonization parameters

Sample ID	**Oxidation Conditions**			**Carbonization Conditions**		
	Hold Temperature (^oC)	**Hold Time (min)**	**Heating Rate (^oC/min)**	**Hold Temperature (^oC)**	**Hold Time (min)**	**Heating Rate (^oC/min)**
B56-800	300	60	1.5	800	120	3
B61	275	60	1.5	1200	120	3
B60	325	60	1.5	1200	120	3
B66	300	30	1.5	1200	120	3
B67	300	90	1.5	1200	120	3
B63.2	300	60	0.5	800	120	3
B64.2	300	60	1	800	120	3
B62.3	300	60	2	800	120	3
B65	300	60	2.5	800	120	3
B73	300	60	3	800	120	3
B74	300	60	3.5	800	120	3
B57	300	60	1.5	1200	120	3
B58	300	60	1.5	1200	120	3
B59	300	60	1.5	1200	120	3
B63-1000	300	60	0.5	1000	120	3
B64-1000	300	60	1	1000	120	3
B56-1000	300	60	1.5	1000	120	3
B62-1000	300	60	2	1000	120	3
B65-1000	300	60	2.5	1000	120	3
B63-1200	300	60	0.5	1200	120	3
B64-1200	300	60	1	1200	120	3

B56-1200	300	60	1.5	1200	120	3
B62-1200	300	60	2	1200	120	3
B65-1200	300	60	2.5	1200	120	3
B56-1500	300	60	1.5	1500	120	3
B72	300	60	1.5	800	120	0.5
B69	300	60	1.5	800	120	1
B71.2	300	60	1.5	800	120	3
B70	300	60	1.5	800	120	5
B68	300	60	1.5	800	120	10
B56.4.72	300	60	1.5	800	120	0.5
B56.4	300	60	1.5	800	120	3
B56.4.68	300	60	1.5	800	120	10

Table A2: Mass changes, XRD and Raman spectroscopy data

	Mass Changes		**Analyses**	
Sample ID	**Oxidation Weight Changes (%)**	**Carbonization Yield (%)**	**D-Spacing (nm)**	I_D/I_G **Ratio**
SVR2-97	N/A	N/A	0.3557	2.21
B56-800	3.37	69.17	0.3932	2.47
B61	2.82	65.05	0.3746	2.20
B60	2.01	63.50	0.3779	2.21
B66	2.04	71.05	0.3733	1.98
B67	3.63	68.40	0.3746	2.04
B63.2	2.10	66.78	0.3922	2.32
B64.2	3.40	63.36	0.3925	N/A
B62.3	2.42	73.59	0.3937	N/A
B65	1.88	72.18	0.3919	2.40
B73	2.22	70.97	0.3895	N/A
B74	-1.88	71.45	0.3864	2.52
B57	3.25	63.23	0.3836	2.15
B58	2.01	59.33	0.3801	2.24
B59	0.33	64.42	0.3751	N/A
B63-1000	3.80	71.51	0.3826	N/A
B64-1000	2.78	72.75	0.3825	N/A
B56-1000	3.41	73.98	0.3840	2.55
B62-1000	2.20	73.76	0.3826	N/A
B65-1000	1.88	72.91	0.3794	N/A
B63-1200	3.80	62.16	0.3751	N/A
B64-1200	2.78	67.24	0.3741	N/A
B56-1200	3.41	66.33	0.3816	2.32
B62-1200	2.20	65.89	0.3751	N/A
B65-1200	1.88	65.18	0.3733	N/A

B56-1500	3.41	35.81	0.3587	1.63
B72	2.74	77.17	0.3867	2.91
B69	2.74	76.80	0.3881	2.76
B71.2	2.74	66.18	0.3923	2.69
B70	2.74	77.17	0.3887	2.79
B68	2.74	76.80	0.3877	2.72
B56.4.72	3.37	74.69	0.3894	2.90
B56.4	3.37	69.17	0.3932	2.63
B56.4.68	3.37	63.27	0.3894	3.05

Table A3: CHNS data

Sample ID	**Elemental Composition**				
	Nitrogen (wt%)	**Carbon (wt%)**	**Hydrogen (wt%)**	**Sulfur (wt%)**	**Est. Oxygen (wt%)**
SVR2-97	1.50	88.52	5.69	3.34	0.95
B60_OX	1.32	74.11	3.19	3.05	18.33
B61_OX	1.41	81.64	4.26	3.28	9.41
B60-1200	0.79	85.24	0.77	3.10	10.11
B61-1200	0.58	73.37	0.62	2.77	22.66
B56.4_OX	1.39	78.50	3.69	3.15	13.27
B56-1200	0.85	84.61	0.58	3.10	10.86
B72-800	1.29	83.40	0.79	1.29	11.62
B69-800	1.27	84.48	0.82	1.27	10.28
B70-800	1.06	78.94	0.78	1.06	16.34
B68-800	1.32	89.49	0.89	1.32	4.65
B71.2-800	1.36	85.13	1.07	1.36	9.09
B56.4.68-800	1.38	85.29	0.82	1.38	8.64
B56.4.72-800	1.32	85.48	0.70	1.32	9.29
B56-800	1.25	83.06	1.32	3.67	10.70
B56-1000	1.28	89.12	0.45	4.37	4.78
B56-1200	0.88	91.27	0.22	3.62	4.02
B56-1500	0.41	95.18	0	2.79	1.63
B74_OX	1.41	81.39	4.24	3.22	9.73
B56.4-800	1.22	83.10	1.33	3.44	10.90
B74-800	1.07	79.58	1.25	2.90	15.20
B63.2-800	1.28	81.91	1.42	3.34	12.05
B66_OX	1.28	77.51	3.74	3.00	14.46
B67_OX	1.36	77.08	3.46	3.15	14.96
B66-1200	0.62	68.71	0.29	2.87	27.50

B67-1200	0.83	90.72	0.54	3.48	4.42
B57-1200	0.83	91.55	0.68	3.48	3.46
B58-1200	0.83	83.86	0.68	3.39	11.24

Appendix B: Sample Calculations

Oxidation Weight Changes Calculations

For example, the sample experienced a $m_{final} = 1.052g$ after oxidation and a $m_{initial} = 1.017g$ before oxidation. The weight changes can be calculated with

$$\%Diff = \frac{m_{final} - m_{initial}}{m_{initial}} \times 100$$

$$\%Diff = \frac{1.052 - 1.017}{1.017} \times 100$$

$$\%Diff = 3.41\%$$

This would equate to the difference in mass after oxidation, which, in this case, is an increase in mass by 3.41%.

Total Yield Calculations

Continuing with the same sample post-carbonization, it experienced a final mass after carbonization of 0.192g after an initial mass of 0.304g before carbonization. To find the yield from the original material, we must also know the final mass after oxidation, which is 1.052g. This is because only some material is used for one carbonization treatment. The yield can be calculated with:

$$\%Yield = \frac{m_{o\_f}}{m_{o\_i}} \times \frac{m_{c\_f}}{m_{c\_i}} \times 100$$

$$\%Yield = \frac{1.052}{1.017} \times \frac{0.192}{0.304} \times 100$$

$$\%Yield = 65.33\%$$

This would equate to a yield of 65.33% after the complete oxidation and carbonization process.

D-Spacing Sample Calculation

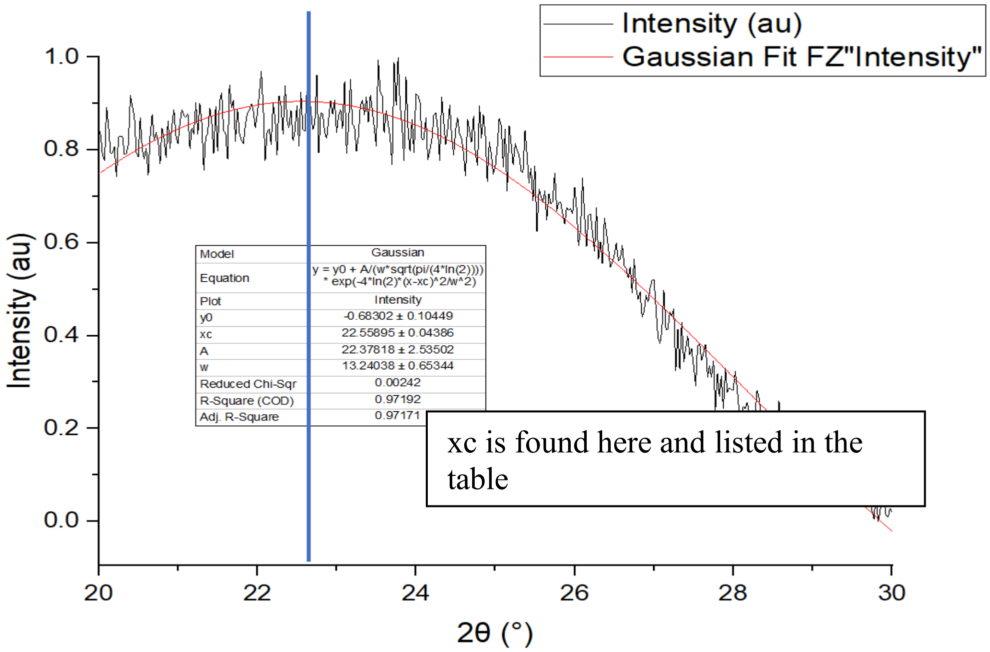

Model	Gaussian
Equation	y = y0 + A/(w*sqrt(pi/(4*ln(2)))) * exp(-4*ln(2)*(x-xc)^2/w^2)
Plot	Intensity
y0	-0.68302 ± 0.10449
xc	22.55895 ± 0.04386
A	22.37818 ± 2.53502
w	13.24038 ± 0.65344
Reduced Chi-Sqr	0.00242
R-Square (COD)	0.97192
Adj. R-Square	0.97171

xc is found here and listed in the table

Figure B1: Sample Gaussian Fitting from XRD Pattern

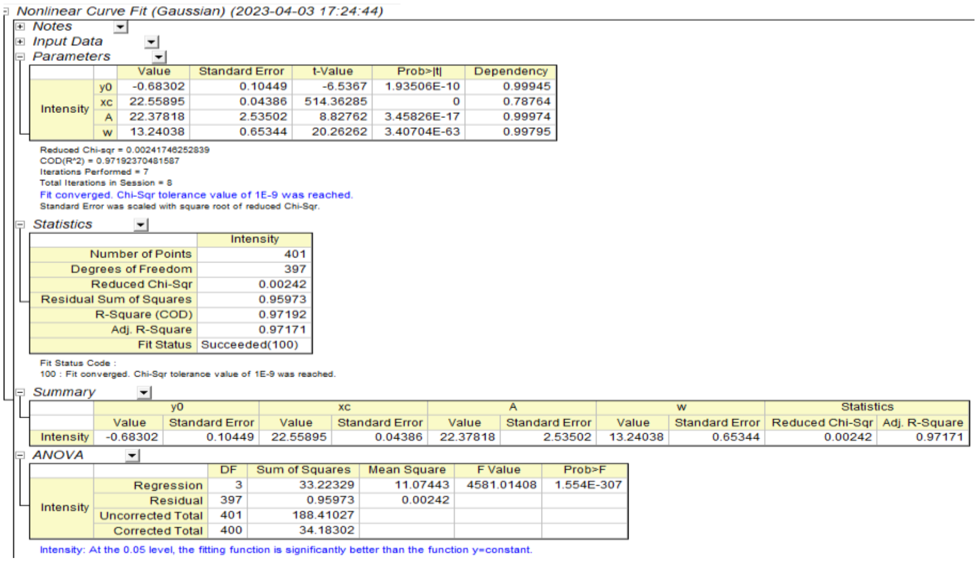

Nonlinear Curve Fit (Gaussian) (2023-04-03 17:24:44)

Parameters

		Value	Standard Error	t-Value	Prob>|t|	Dependency
Intensity	y0	-0.68302	0.10449	-6.5367	1.93506E-10	0.99945
	xc	22.55895	0.04386	514.36285	0	0.78764
	A	22.37818	2.53502	8.82762	3.45826E-17	0.99974
	w	13.24038	0.65344	20.26262	3.40704E-63	0.99795

Reduced Chi-sqr = 0.00241746252839
COD(R^2) = 0.97192370481587
Iterations Performed = 7
Total Iterations in Session = 8
Fit converged. Chi-Sqr tolerance value of 1E-9 was reached.
Standard Error was scaled with square root of reduced Chi-Sqr.

Statistics

	Intensity
Number of Points	401
Degrees of Freedom	397
Reduced Chi-Sqr	0.00242
Residual Sum of Squares	0.95973
R-Square (COD)	0.97192
Adj. R-Square	0.97171
Fit Status	Succeeded(100)

Fit Status Code :
100 : Fit converged. Chi-Sqr tolerance value of 1E-9 was reached.

Summary

	y0		xc		A		w		Statistics	
	Value	Standard Error	Value	Standard Error	Value	Standard Error	Value	Standard Error	Reduced Chi-Sqr	Adj. R-Square
Intensity	-0.68302	0.10449	22.55895	0.04386	22.37818	2.53502	13.24038	0.65344	0.00242	0.97171

ANOVA

		DF	Sum of Squares	Mean Square	F Value	Prob>F
Intensity	Regression	3	33.22329	11.07443	4581.01408	1.554E-307
	Residual	397	0.95973	0.00242		
	Uncorrected Total	401	188.41027			
	Corrected Total	400	34.18302			

Intensity: At the 0.05 level, the fitting function is significantly better than the function y=constant.

Figure B2: Sample Results Table from Gaussian Nonlinear Curve Fit

Given an xc location of 22.56° from the Gaussian line fitting in Figure B2, we can calculate θ.

$$\theta = \frac{xc}{2}$$

$$\theta = \frac{23.49073}{2}$$

$$\theta = 11.745365^{\circ}$$

This can then be plugged into Bragg's law equation with a wavelength corresponding to the copper radiation source of the XRD, which corresponds to 1.5406Å.

Therefore,

$$d_{(002)} = \frac{\lambda}{2sin\theta}$$

$$d_{(002)} = \frac{1.5406}{2\sin{(11.745365)}}$$

$$d_{(002)} = 3.7841\text{Å}$$

$$d_{(002)} = 0.3784nm$$

Elemental Composition Calculations

Table B1: Sample Elemental Composition

Weight Measured (g)	**Elemental Composition**					
	Nitrogen (wt%)	**Carbon (wt%)**	**Hydrogen (wt%)**	**Sulfur (wt%)**	**Sum (wt%)**	**Estimated Oxygen (wt%)**
2.41	1.22	83.10	1.33	3.44	89.10	10.90

The H/C and (NOS)/C ratios can be calculated for the sample with the elemental composition corresponding to Table B1.

Given the molar masses:

Carbon	12.01 g/mol
Hydrogen	1.01 g/mol
Nitrogen	14.01 g/mol
Sulfur	32.07 g/mol
Oxygen	16.00 g/mol

H/C Calculations:

$$\frac{H}{C} = \frac{n_H}{n_C} = \frac{m_H}{m_C} \times \frac{M_H}{M_C}$$

$$\frac{H}{C} = \frac{(2.41)(\frac{1.33}{100})}{(2.41)(\frac{83.10}{100})} \times \frac{1.01}{12.01}$$

$$\frac{H}{C} = 0.191$$

NOS/C Calculations:

$$\frac{NOS}{C} = \frac{n_N + n_O + n_S}{n_C} = \frac{m_N + m_O + m_S}{m_C} \times \frac{M_N + M_O + M_S}{M_C}$$

$$\frac{NOS}{C} = \frac{(2.41)\left(\frac{1.22}{100}\right) + (2.41)\left(\frac{10.90}{100}\right) + (2.41)\left(\frac{3.44}{100}\right)}{(2.41)(\frac{83.10}{100})} \times \frac{(14.01 + 16.00 + 32.07)}{12.01}$$

$$\frac{NOS}{C} = 0.1266$$

This sample has a H/C ratio of 0.191 and a (NOS)/C ratio of 0.1266.

Ratio Calculations with Raman Spectroscopy

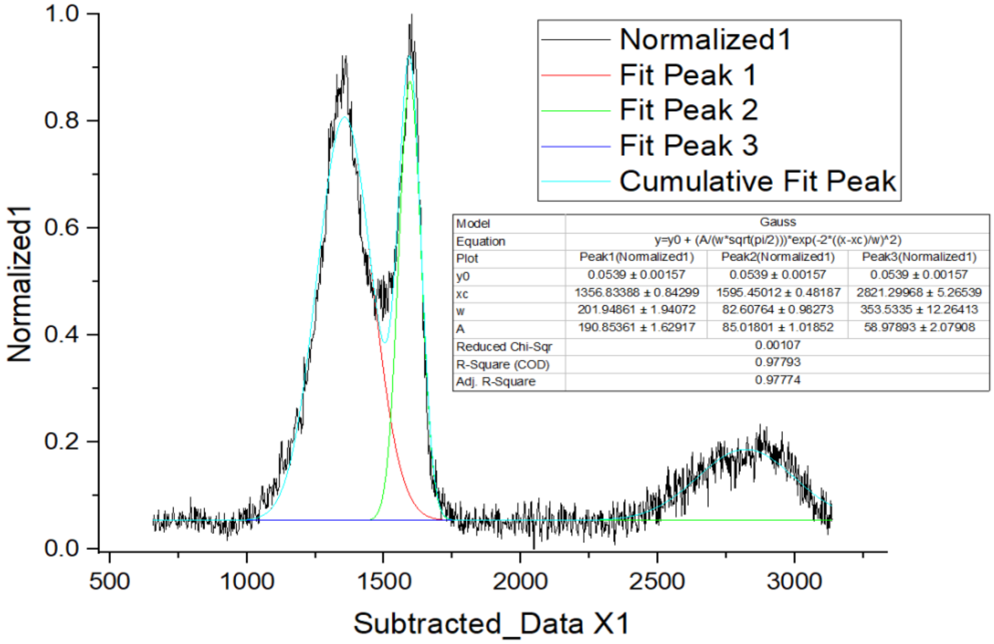

Model	Gauss		
Equation	y=y0 + (A/(w*sqrt(pi/2)))*exp(-2*((x-xc)/w)^2)		
Plot	Peak1(Normalized1)	Peak2(Normalized1)	Peak3(Normalized1)
y0	0.0539 ± 0.00157	0.0539 ± 0.00157	0.0539 ± 0.00157
xc	1356.83388 ± 0.84299	1595.45012 ± 0.48187	2821.29968 ± 5.26539
w	201.94861 ± 1.94072	82.60764 ± 0.98273	353.5335 ± 12.26413
A	190.85361 ± 1.62917	85.01801 ± 1.01852	58.97893 ± 2.07908
Reduced Chi-Sqr	0.00107		
R-Square (COD)	0.97793		
Adj. R-Square	0.97774		

Figure B3: Sample Gaussian Fitting for Raman Spectroscopy

The defect ratio can be calculated since the area returned for the intensity of the defect band is 190.85, and the area of the graphitic band is 85.02 after a Gaussian line fitting. The areas correlate to the A values for peaks 1 and 2 in Figure X.

$$Ratio = \frac{I_D}{I_G}$$

Where

- ID = area under curve for d-band
- IG = area under the curve for g-band

$$Ratio = \frac{190.85}{85.02}$$

$$Ratio = 2.25$$

This results in a sample with a defect ratio of 2.25.